

N 70 15207

UTEC DO 69-150

November 1969

NASA CR 107561

COHESIVE AND ADHESIVE POLYMER FRACTURE INVESTIGATION

by

William Benjamin Jones, Jr.

This Ph.D. Dissertation was funded by
the National Aeronautics and Space Administration
under

Grant NGR 45-003-029

**CASE FILE
COPY**

College of Engineering
University of Utah
Salt Lake City, Utah

UTEC DO 69-150

November 1969

COHESIVE AND ADHESIVE POLYMER FRACTURE INVESTIGATION

by

William Benjamin Jones, Jr.

This Ph.D. Dissertation was funded by
the National Aeronautics and Space Administration
under
Grant NGR 45-003-029

College of Engineering
University of Utah
Salt Lake City, Utah

COHESIVE AND ADHESIVE POLYMER FRACTURE INVESTIGATION

by

William Benjamin Jones, Jr.

A dissertation submitted to the faculty of the
University of Utah in partial fulfillment
of the requirements for the degree of

Doctor of Philosophy

Department of Mechanical Engineering

University of Utah

June 1970

ACKNOWLEDGEMENTS

It is with great pleasure that the author acknowledges the support of those who have made this dissertation possible.

The author is indebted to Dr. M. L. Williams for his valuable guidance and constructive suggestions.

Appreciation is expressed to Dr. K. L. DeVries for the many enlightening discussions and his helpful suggestions during the preparation of this thesis.

The author wishes to express thanks to the National Aeronautics and Space Administration for financial support of this research.

Appreciation is also expressed to Mr. Mike Beeley and Mr. Frank Selto for assistance with the experimental work and to Mrs. Marvel Leader and Mrs. Jo Broadbent for the preparation of this manuscript.

TABLE OF CONTENTS

	page
ACKNOWLEDGEMENTS	iii
TABLE OF CONTENTS	iv
LIST OF FIGURES	vi
LIST OF TABLES	viii
ABSTRACT	ix
I. INTRODUCTION	1
1.1 Historic Background	1
1.2 Continuum Approach to Adhesive Fracture	8
II. THE SPHERICAL/CYLINDRICAL FLAW APPROACH TO COHESIVE FRACTURE	16
2.1 Spherical Flaw in Viscoelastic Media	18
2.2 Loading functions Which are Sums of Simple Loading Functions	23
2.3 Cyclic Fatigue--Spherical Flaw/Cylindrical Flaw	24
2.4 Cyclic Fatigue--Cylindrical Flaw Tests	29
2.4.1 Test Apparatus and Procedure.	29
2.4.1.1 Apparatus	30
2.4.1.2 Procedure	32
2.4.2 Heat Transfer Analysis	34
2.4.3 Discussion of Data	38
2.4.4 Fracture Surface Examination	41
III. ADHESION	46
3.1 Analytical Developments	46
3.2 Blister Peel Tests	55
3.2.1 Experimental Observations	57
3.3 Problematic Approach	59
3.3.1 Solid Rocket Problem	60
3.3.2 Fiber Pull Out Problem	65
IV. CONCLUSIONS	68

TABLE OF CONTENTS (continued)

	page
4.1 Cohesive Viscoelastic Fracture	68
4.2 Adhesive-Elastic Fracture	69
V. LIST OF REFERENCES	70
VI. APPENDIX A.	74
VII. APPENDIX B.	80
VIII. VITA	105

LIST OF FIGURES

Figure		page
1	Comparison of the propagating flaw solutions for two loading conditions	81
2	Dependence of fatigue life on frequency for viscoelastic material	81
3	Dimensions of test specimen	82
4	Test Machine	82
5	Observation Angle	83
6	Crack length versus number of cycles for simple tension fatigue tests on Solithane 113. .	84
7	Temperature near crack tip vs. fatigue cycles with multiple frequencies and sequence reversal upper curve at 4000 c/m then 800 c/m; lower curve at 800 c/m then 4200 c/m	85
8	W L F Curve for GALCIT I	86
9	$E''(\omega)$ (loss modulus) vs. frequency curve for GALCIT I	86
10	Estimated temperature rise vs. time for a viscoelastic sample in uniaxial cyclic fatigue ($\omega < \omega_m$)	87
11	Estimated change of fatigue life at constant frequency due to temperature increase	87
12	Comparison of fatigue life for fan cooled and uncooled samples	88
13	Optical microphotograph of GALCIT I fatigue fracture surface (100x)	89
14	Optical microphotograph showing surface effects of dual frequency fatigue (100x)	89

Figure		page
15	Transmission electron microscopic photograph showing fatigue striations (13,500x)	90
16	River markings resulting from a tear test (70x)	90
17	Tear Fracture surface from an incomplete fatigue test (120x)	91
18	Sketch of the deflected plate	92
19-a	Photograph of blister test apparatus	93
19-b	A blister test in progress.	93
20	Typical pressure versus deflection test data	94
21	Plot of the critical pressure versus center deflection from a blister test	94
22	Axisymmetric finite element model of a propellant grain	95
23	Strain energy vs. area for various end conditions	96
24	Critical pressure vs. crack length for bond failure	97
25	Strain energy versus area for acceleration loading	98
26	Inverse square root of energy release rate for acceleration loading	99
27	Finite element grid for fiber pull out problem	100
28	Schematic of area release on filament problem	101
29	Strain energy versus release area on filament problem	101
30	Profile of hypothesized unbonds in axisymmetric body	102
31	Energy release for the fiber pull out problem	103

LIST OF TABLES

	PAGE
Table 1 Stress Intensity Factors for Various Geometries	75
Table 2 Constant Frequency Tests	77
Table 3 Multiple Frequency Tests	78
Table 4 Average Cycles to Failure	79

ABSTRACT

Previous investigators have demonstrated the similarities of cohesive and adhesive fracture through continuum mechanical energy approaches. These approaches have been applied to viscoelastic cohesive fatigue fracture problems and to elastic adhesive fracture analyses. Experimental results graphically illustrate the need for thermomechanical coupling considerations in viscoelastic fatigue fracture predictions. An adhesive fracture test method was developed that verified the analytical predictions and also has engineering applications for evaluation of bond strengths. Some applications are demonstrated by examples of a solid rocket motor and a filament withdrawn from a surrounding matrix.

I. INTRODUCTION

Even from earliest times, as man began to reshape his environment, to implement naturally occurring materials as tools, weapons and protective structures, he has been plagued by fracture were made useless by impact fracture. Roman soldiers became defenseless when their bronze sword blades fractured against the steel blades of Damaskians. Priceless stone art objects were fractured by careless handling. More recently, many lives have been lost because of fracture in bridge structures, automobile, airplane and construction components. As greater reliance is placed on structural extensions of man's abilities, it is increasingly important that fracture be understood and controlled.

1.1 HISTORIC BACKGROUND

Probably one of the first significant observations that led to a better understanding of fracture came when Galilei⁽¹⁾ attempted to measure the strength of iron bars. Through very arduous labor, he made and loaded a number of bars of different lengths to failure. He observed that their strength was inversely proportional to length. This was a surprise. It had been previously recognized that the force necessary to break a specimen was linearly proportional to the size or cross-sectional area. But this length dependence--was it a new phenomenon?

Progress was slow, thinking clouded by superstition, but eventually it was recognized that all technical materials contain flaws and that these flaws influence fracture. Once flaws were recognized, Galilei's work could be re-examined. His manufacturing techniques were crude

and each of his bars contained flaws, some more than others. From a statistical approach, quantitized by Weibull,⁽²⁾ the longer the bar, the greater the probability of containing a large flaw. Then it was understood that Galilei's experiments were influenced by the distribution of flaws, not by length.

Several investigators developed qualitative ideas about fracture and stress/strain criteria for fracture developed. In 1913, Inglis⁽³⁾ developed a stress analysis for a large plate containing an elliptic hole, which in the limit became a sharp crack. It was not until Griffith⁽⁴⁾ added his energy balance concept to the Inglis work that brittle or elastic fracture was quantitatively described.

Before Griffith, the concept of stress/strain was used as failure criteria. The technique, much the same as today, was to consider a structure, calculate the stress/strains in the loaded structure, and then compare these calculated values with measured ultimate tensile strength of the material. The solution developed by Inglis predicted infinitely high stresses at the tip of a sharp crack, regardless of the magnitude of the applied (positive) load. So comparisons of this predicted stress value to measured ultimate values become meaningless. Griffith recognized that while the calculated stress was mathematically singular, the distribution was proportional to the inverse square root of the distance from the crack tip and the resulting strain energy was finite and calculable. He then postulated that there is a characteristic fracture energy associated with creating new surface, and demonstrated how an energy balance could be made for a sheet of brittle material (glass) containing a crack and how the critical stress (just large enough to cause

the pre-existing crack to grow) depends upon that fracture energy. From fracture experiments made using glass, the fracture energy was calculated. Independent experiments to determine the surface energy were conducted at elevated temperatures by hanging weights midspan on thin glass fibers supported at either end. The surface energy and the fracture energy were found to be approximately equal and it was deduced that other dissipative mechanisms were negligible in the fracture of glass.

In principle, Griffith's energy balance concept is valid. It gives the accurate functional relationship between the applied stress at fracture and flaw size for brittle materials, and gives favorable comparisons between predicted cohesive strength in defect free material and experimentally determined strengths for single crystal whiskers. In practice, Griffith's concept gives adequate approximations for fracture analysis of many engineering materials, however, difficulties are encountered when the concept, developed for brittle materials, is applied to ductile materials⁽⁵⁾ due to the elusiveness of the value of the fracture energy and to the lack of crack length sensitivity. Investigators⁽⁶⁾ of metal fracture object that the Griffith concept represents an oversimplification of a series of much more complicated phenomena in an age when there is no need to resort to such a gross oversimplification. Many investigators then turned to microscopic and atomic scale models with the development of the Dislocation Theory in 1934. Through models of atomic stacking faults, dislocation movement, twinning, etc. many features of metal behavior were described. These studies have produced valuable results, including explanations of the development of sharp cracks in an initially "flaw free" material (see Cotterell-Hull⁽⁷⁾). At present these studies are incomplete and a loop has not closed between dislocation studies and a global energy approach to fracture.

In 1945, Orowan⁽⁸⁾ reported that x-ray analysis showed extensive plastic deformation on the fracture surfaces of materials which had failed in "brittle fashion." Then in 1948, Irwin⁽⁹⁾ pointed out that the Griffith type energy balance must be between the strain energy stored in a specimen and the surface energy plus the work done in plastic deformation. Further work by Orowan⁽⁸⁾ elucidated the manner of treating plastic deformations and demonstrated that the modified Griffith condition for fracture is not only a necessary but also a sufficient condition for crack propagation. It resulted that the fracture energy was the sum of the surface energy and the plastic work.

The stress criteria to fracture has persisted. Stress field expansions for crack tips given by Sneddon⁽¹⁰⁾ have been extended by Irwin⁽¹¹⁾ and Williams⁽¹²⁾ in general for any isotropic elastic body. The local stresses near the crack tip may be expressed in terms of a parameter K which is designated the "Stress Intensity Factor," Irwin⁽¹¹⁾ showed that for elastic materials the energy approach is equivalent to the stress intensity approach. Linear theory of elasticity provides unique and single valued relationships among stress, strain, and energy. Therefore, an energy fracture criterion has its equivalent stress and strain criteria, all of which are mathematically indistinguishable. For materials exhibiting plastic flow, however, such is not the case.

Analytical solutions have been developed for elastic-plastic materials in shear by Hult and McClintock⁽¹³⁾. For crack opening in simple tension, approximate methods are being used. For instance, recently Folias⁽¹⁴⁾, using the Dugdale⁽¹⁵⁾ model (a narrow band of plastic deformation preceding the crack front) has successfully demonstrated a manner in which plastic flow may be included in fracture

analyses of curved plates.

Returning to the energy approach, a pattern begins to emerge. There is nothing basically wrong with an energy approach, but whereas Griffith was able, in assuming brittle behavior, to balance the energy interchange between elastic strain energy and surface energy, treatment of non-brittle materials necessitates consideration of additional dissipative energies. Irwin⁽⁹⁾ emphasized that all energy dissipated as a fracture progresses, including that not directly related to the formation of new surface area, must be considered. Within this framework, it appears all materials may be included, even those with time dependent material properties. For example, if one were to inquire about application to viscoelastic materials, the major dissipative mechanism is internal damping.

Many materials, including the organic polymers, exhibit complex behavior. Frequently polymeric materials are described as being viscoelastic at temperatures above their glassy transition temperature and elastic below that transition temperature. Such generalizations can be deceptive; for example, polymethyl-methacrylate (PMMA) and polystyrene have glassy transition temperatures well above room temperature and are frequently referred to as organic glasses. Fracture investigation for these materials, closely paralleling those in metals,⁽¹⁶⁾ have shown plastic flow work terms about 10^3 times greater than the surface energy. Hence, energy considerations must include plastic work terms in the glassy region of these, and probably most, polymeric materials. It is not clear at the moment whether viscoplastic considerations must also be carried through the transition regions for such materials.

Rivlin and Thomas⁽¹⁷⁾ in an extension of the Griffith theory propose that fracture impends when

$$-\left. \frac{\partial U}{\partial A} \right| = T \quad (1.1)$$

where T is a characteristic energy density

U = elastic stored energy

A = crack area

and where the subscript $|$ indicated no further work is done during the interchange of stored energy to surface energy. Similar results were used by Berry⁽¹⁸⁾ for initiation of an edge crack configuration. Rivlin and Thomas were careful to emphasize that dissipation, other than surface energy, could occur during the fracture process.

Williams⁽¹⁹⁾ observed that for a conservative system, the energy balance consists of separating the energy input into its various output components. In the simple brittle case considered by Griffith, the deformations are all presumably elastic and the work put into the system is dissipated or transferred into the work of creating new surface. For a propagating crack, kinetic energy must also be considered. For more complicated material behavior, appropriate dissipative energy terms such as plastic work and viscoelastic dissipation are included. Since these terms are all scalar energies, the resulting critical stress may be expressed as

$$\sigma_{cr} = k \sqrt{\frac{E}{a} \sum T_i} \quad (1.2)$$

where k is constant for the geometry considered, E is the material modulus, a is the half crack length and $\sum T_i$ reflects the summation of the dissipative processes in the material. For brittle, ductile,

and viscoelastic materials, respectively, one would insert T_b , T_d , and T_v . For brittle materials, in which $T_b \gg T_d + T_v$, one recovers the Griffith relation.

Experimental evidence led to more careful consideration of the dissipative mechanisms in viscoelastic fracture. In order to elucidate the viscoelastic dissipative influences on fracture, Williams⁽¹⁹⁾ has chosen a spherical flaw model which will be described more completely later.

It was found that the critical stress was predictable in terms of a geometric factor, viscoelastic compliances to account for viscous dissipation, and the surface energy density. This is a particularly significant contribution since the viscous dissipation enters through a time and hence a load history dependence.

The spherical flaw model appeared to be such a convenient device for exploring the implications of viscoelastic fracture that Williams et al.^(20, 21) utilized it in a study of isothermal cumulative damage. Certain parts of this study are offered in this thesis as contributions to a better understanding of cumulative damage in a linearly viscoelastic material.

More recently Noel, Burton and Harbert⁽²²⁾ have investigated cumulative damage in a viscoelastic rocket fuel. Analyses were extended using the spherical flaw model to predict propellant behavior under a variety of loading histories. Their experimental results, however, were somewhat clouded by the inapplicability of linear viscoelastic constitutive relations to the solid propellant. The implications of viscoelasticity are that loading and hence damage

effects decay with time or that the material displays a fading memory. For the material studied, permanent damage was experienced. Continuum mathematical models may be fitted to experimentally determined response for composite materials. Such permanent damage is currently being considered in the development of more general constitutive relations by Farris.⁽²³⁾

There are certain similarities to be noted between cohesive and adhesive fracture. Analytical developments from continuum mechanics describe stress singularities, albeit of different types, for crack tips whether these cracks lie imbedded within a single material, or along an interface between two materials. The energy approach neatly circumvents the difficulties experienced in cohesive fracture analysis and appears applicable to adhesive fracture analysis.

1.2 CONTINUUM APPROACH TO ADHESIVE FRACTURE

With the increasingly frequent use of adhesives to join dissimilar materials, it is important to understand and to be able to predict adhesive fracture. Adhesive fracture studies have ranged from the atomic structure viewpoint through global energy balance based on continuum mechanics. While the latter approach will be taken, it is appropriate to review some of the results of atomic approaches.

Adhesion may be defined as the state in which the surfaces of two materials are held together by interfacial forces. An adhesive is a material or substance capable of holding materials together by surface attachments. These definitions are quite general and often ambiguous. For that matter, the term adhesive may not be necessary academically since a thin film of material may affect adhesion with a material surface on the one side, and also may affect adhesion with another and possibly different material surface on the other side.

However, to remain consistent with the voluminous quantities of literature on the subject, the above definitions will be used to describe the state in which a material is held together by internal forces. If a piece of material is pulled apart, these cohesive forces must be overcome. If then, these pieces are physically rejoined without intentionally introducing a binding medium (adhesive), it is in a state of autoadhesion. If however, one of the pieces is joined to a different material, then adhesion is said to exist. It is easily envisioned that in the joining of two pieces of material, surface roughness and contamination such as dust, air, or oil, will influence the proximity of atoms across the interface, and hence, if the forces are dependent upon proximity, the forces.

This indeed is the case. On the atomic scale, forces that have been defined include:⁽²⁴⁾

1) Primary bonds

- a) Ionic bonds develop between the atoms of certain dissimilar elements when one element possesses easily detachable valence electrons and the other element requires additional electrons to fill an electron shell.
- b) Covalent bonds are said to exist when atoms of certain elements have a tendency to share some of their valence electrons.
- c) Metallic bonds also result from sharing of valence electrons, except these electrons may circulate freely within the body, forming a kind of electron cloud that holds the positively charged ions together in a close-packed configuration.

2) Secondary (intermolecular, Van der Waals) bonds⁽²⁵⁾

Even though the valency forces of atoms are saturated within a molecule, molecules still attract each other with much weaker forces. These forces, arising from permanent or induced dipoles may be divided into three known groups. The effects are named after the respective investigators.

- a) The Keesom effect (also orientational effect)--Attractive forces may be observed between two molecules with permanent dipole moments. Keesom⁽²⁶⁾ found the energy of attraction for two like molecules of dipole moment μ , is given by

$$V_{\text{Keesom}} = - \frac{2 \mu^4}{3 k T r^6} \quad (1.3)$$

where k = Boltzmann constant

T = temperature

r = distance between molecules.

For dissimilar molecules of dipole moments μ_1 and μ_2

$$V_{\text{Keesom}} = - \frac{2 \mu_1^2 \mu_2^2}{3 k T r^6} \quad (1.4)$$

- b) The Debye effect⁽²⁷⁾--During experimental investigations at relatively high temperatures, Debye observed molecular attractions that could not be attributed to the Keesom effect. He concluded an additional attractive effect existed and was the result of polarizing action or

induced dipoles. The mutual attractive potential energy for two like molecules was found to be

$$V_{\text{Debye}} = - \frac{\alpha \mu^2}{r^6} \quad (1.5)$$

where α is the polarizability of the molecule. For two different molecules, the expression becomes

$$V_{\text{Debye}} = - \frac{\alpha_1 \mu_2^2 + \alpha_2 \mu_1^2}{r^6} \quad (1.6)$$

- c) The London effect⁽²⁸⁾ --London pointed out that if, instead of considering the time average effect and considering instead an instantaneous picture of the molecules, various electronic configurations could exist. Thus, for short time intervals, the molecules would possess dipoles, which would act upon neighboring molecules and induce dipoles in them. The consequence of such an interaction is an attraction between molecules. London found by a quantum mechanical treatment of the problem that the mutual attractive potential energy was given by the expression:

$$V_{\text{London}} = - \frac{3}{4} \frac{h \nu_o \alpha^2}{r^6} \quad (1.7)$$

where h = Plancks constant

ν_o = the characteristic frequency of the molecule.

For two molecules of polarizabilities α_1 and α_2 and

characteristic frequencies ν_1 and ν_2 the expression becomes

$$V_{\text{London}} = -\frac{3}{2} \frac{h \nu_1 \nu_2}{\nu_1 + \nu_2} \frac{\alpha_1 \alpha_2}{r^6} \quad (1.8)$$

Another important conclusion reached by London was that this effect is simply additive, i.e., the simultaneous interaction of many molecules can simply be built up as an additive superposition of single forces between pairs. The London effect is always large in comparison to the other effects mentioned and, except for the most polar molecules, appears to predominate.

- 3) Hydrogen bonding. Some authors⁽²⁹⁾ prefer to categorize hydrogen bonding with Van der Waals forces, while others, because of the significant role hydrogen bonding plays in polymeric materials, prefer to treat it under a separate heading. Whichever the case, hydrogen plays a somewhat unique role since it can exist both as a positively charged and as a negatively charged ion. The negative ion is formed by imperfect shielding of the positively charged nucleus by the single electron in a neutral atom. This imperfect shielding will result in a constantly shifting dipole which has a weak tendency to acquire another electron by purely ionic attraction. This property of the hydrogen atom enables it to bridge two negative ions, in what is known as hydrogen bonding.

The binding forces in elements and chemical compounds are usually mixtures of the idealized types discussed above. To get a feel for the contribution of each type bonding,⁽²⁴⁾ it is interesting to note that primary bonds usually have an energy of 2 to 10 electron volts (ev)/atom, while the energy for hydrogen bonding is between 0.2 and 0.5 ev/atom and for secondary or Van der Waals bonding is 0.02 to 0.2 ev/atom.

More detailed discussions of the binding forces and adhesion in general are found in texts by Houwink and Salomon⁽³⁰⁾ and by Patrick.⁽²⁹⁾

A necessary part of the approach for establishing strong bond joints and for developing good adhesion is a study of atomic and chemical interactions. However, the gap has not been bridged so that atomic scale models can be used quantitatively for fracture analysis. Although relating of microscopic force interactions to macroscopic fracture would be an important contribution, the author has chosen a simpler approach by considering the continuum representation

It has been pointed out by Williams,⁽³¹⁾ that from the viewpoint of continuum mechanics, and particularly the energy concept of fracture, adhesive and cohesive failures are similar. The essential difference involves the interpretation of the energy required to create new (adhesive or cohesive) surface area. It is recognized that technical adhesive interfaces as well as real materials contain flaws, and that these flaws (sharp geometric discontinuities) give rise to mathematical stress singularities.

Consider, for example, a crack of finite length, $2a$, centrally located in a large sheet, say along the x -axis. If the material above and below the axis is the same, this becomes the Griffith problem

with stress singularities at $x = \pm a$. Now consider the material in the upper half plane to be incompressible and the material in the lower half plane to be rigid and then assume perfect adhesion over $|x| > a$. Again the stresses at the crack ends, $x = \pm a$, are singular. In the first case the Griffith energy approach, involving integration of the stress squared over the area of the specimen, provides the solution to a well known and classical example of cohesive fracture. The second case is an example of perfect adhesive fracture. Suffice it to say just now that for an edge-bonded specimen having a central finite crack at the interface with a rigid boundary, a stress analysis can be conducted and the incremental new surface energy generated can be calculated as the crack extends.

In addressing adhesion problems, it is necessary to inquire which problems have integrable stress singularities. Williams⁽³²⁾ has defined certain cases, and Malyshev and Salganik⁽³³⁾ referring to these descriptions have run tests to evaluate surface energies for the bond of PMMA to steel. Earlier Dannenberg⁽³⁴⁾ forced mercury between a polymeric coating and a stiff plate to determine the work necessary to debond a fixed area, but did not discuss the strain energy balance. More recently, Williams⁽³¹⁾ has shown the singularity for a crack tip being precisely along the interface between a rigid material ($E \rightarrow \infty$) and an incompressible material ($\nu = 0.5$) is well behaved (i.e., integrable), and further has suggested a pressurized blister configuration as a convenient means of measuring adhesive surface energy density. Using the blister configuration, the author has

conducted a number of tests. These tests and certain analyses will be described later.

The various dissipative mechanisms have been discussed and references cited for the manner of including these mechanisms into an energy balance. Simplified geometries have been mentioned that reduce the mathematical complexity of the problems so that attention may be focused on the influence of material behavior. While microscopic and atomic scale studies are necessary for complete understanding of fracture phenomena, the value of single parameter fracture criteria can not be disputed. Using the energy balance on continua, such fracture relations will be developed for certain cases of cohesive viscoelastic fracture and elastic adhesive fracture.

II. THE SPHERICAL/CYLINDRICAL FLAW APPROACH TO COHESIVE FRACTURE

The stress intensity factor approach to fracture has shown some very interesting features about the analytical treatment of stress singularities. For a large class of problems, it has been shown that the stresses near a singularity are expressed by⁽¹¹⁾

$$\sigma_{ij} = \frac{K_I}{\sqrt{2\pi r}} f_{ij}(\theta) \quad (2.1)$$

where $\sigma_{ij}(r, \theta)$ are the various stress components at a distance r from crack tip and an angle θ from crack plane.

K_I = stress intensity factor for crack opening mode, I.

For an elastic body, Irwin⁽¹¹⁾ has shown an equivalence between the stress intensity factor approach and the energy rate approach from which he arrives at an energy rate, \mathcal{G} ;

$$\mathcal{G}_I = \left. \frac{dU}{dA} \right|_{\text{fixed grips}} = \frac{K_I^2}{E} \quad \text{plane stress} \quad (2.2)$$

$$\mathcal{G}_I = \frac{(1 - \nu^2) K_I^2}{E} \quad \text{plane strain} \quad (2.3)$$

and further, for complex loading conditions;

$$\mathcal{G} = \frac{1 - \nu^2}{E} (K_I^2 + K_{II}^2) + \frac{1 + \nu}{E} K_{III}^2 \quad (2.4)$$

where K_{II} and K_{III} are stress intensity factors for edge sliding and tearing modes respectively. But when the loads are such that fracture just impends or at criticality, the energy rate term is recognizable from

the energy balance relations previously described as the rate of doing surface work with surface area. Surface work may also be described as

$$SE = \int_0^A \gamma_c dA \quad (2.5)$$

where γ_c = surface work/unit area

A = surface area

then, at the critical load for crack growth

$$\frac{d}{dA} (SE) = \gamma_c = G_{cr} \quad (2.6)$$

It can be shown for the classical Griffith problem of a centrally located crack in an infinite sheet loaded by simple tension that

$$\gamma_c = \frac{K_{cr}^2}{2E} \quad (2.7)$$

where the cr-subscript on the stress intensity factor indicates criticality, and c-subscript on the surface work density term denotes cohesive fracture.

The critical stress intensity factor is then recognizable as a material property. But from the stress intensity factor approach, the relation of this factor to the load imposed far from the crack, and the crack and body geometry can be expressed.

While there is yet to be a completely unified cataloguing of stress intensity factors, many are listed by Paris and Sih⁽²⁵⁾ and shown by McClintock and Argon.⁽²⁴⁾ Several of these are listed in

Table 1. The inference drawn by Williams is that because the geometric contributions are separable from the material properties, e.g., the stress intensity factor is a material property, influences of material properties changes can be studied using the most simple available geometry, then results extended to other configurations using the appropriate geometric factors. In pursuit of this approach, it became apparent one of the simplest geometries is a sphere of outer radius, b , containing a concentric spherical flaw of radius a . For uniform loading or displacements of the outer boundary, it is seen that the problem is one dimensional in radius r . Fracture is assumed to take place uniformly around the surface of the spherical flaw (radius a). Physically, this fracture surface configuration is highly improbable, but would more than likely be a ring extending from the spherical surface similar to attached Saturn rings;⁽³⁶⁾ however, if the stress intensity interpretation may be extended, the physically observable fracture surface development could be analytically described using the appropriate geometric factor, thence the assumed uniform spherical fracture surface extension is valid for studying the phenomenological influence of material behavior on fracture.

2.1 SPHERICAL FLAW IN VISCOELASTIC MEDIA

Fracture criticality conditions for a spherical flaw in a linear viscoelastic incompressible material have been calculated for a number of loading conditions.⁽¹⁹⁾ It will be informative to review a few of these developments and results.

For stress boundary conditions, the energy balance conditions are satisfied by

$$\dot{a} \left\{ -\frac{\sigma_o^2}{a^4} \int_0^+ S(\xi) \frac{\partial}{\partial \xi} \left[D_g S(\xi) + \int_0^\xi \frac{\partial D_{crp}(\xi-\tau)}{\partial(\xi-\tau)} S(\tau) d\tau \right] d\xi + 2a\gamma \right\} = 0 \quad (2.8)$$

where σ_o = normalized stress applied at outer boundary

a = radius of flaw

ξ, τ, t = time variables

D_g = glassy compliance

$D_{crp}(t)$ = creep compliance

γ = cohesive fracture energy per unit area.

$$S(t) = -\frac{3}{2} \frac{a^3(t) f(t)}{1 - \left[\frac{a(t)}{b} \right]^3} \quad (2.9)$$

$$\sigma(t) = \sigma_o f(t)$$

It is noted that equation (2.8) is satisfied for no fracture, i.e., $\dot{a} = 0$ and also when the bracketed term is zero. Both terms are useful in determining criticality conditions.

Using the bracketed term of equation (2.8) for a step applied stress ($\sigma(t) = \sigma_o$ for $t \rightarrow 0$) it is found that

$$\sigma_{ocr} = \frac{4}{3} \sqrt{\frac{\gamma_c}{a_o (2D_{crp}(t_o) - D_g)}} \quad (2.10)$$

where $\frac{a}{b} \ll 1$.

This demonstrates that for a constant surface energy, the

critical stress decays with time, with the upper limit occurring as the time after load application, t_o , approaches zero. As $t_o \rightarrow 0$, then $D_{crp}(t_o) \rightarrow D_g$. Since $D_g = \frac{1}{E_g}$, it is found that

$$\sigma'_{ocr} = \frac{4}{3} \sqrt{\frac{E_g \gamma_c}{\alpha_o}}$$

Thus, if a step stress less than σ'_{ocr} were applied, one would expect failure to occur at some finite length of time, as long as that applied stress is greater than the lower limit that corresponds to the rubbery modulus (i.e., equation (2.10) with $D_{crp} \rightarrow \frac{1}{E_r}$ for very long times).

For displacement boundary conditions the energy balance yields

$$\dot{a} \left\{ 2a\gamma - \frac{4b^6}{a} \left(\frac{u_o}{b} \right)^2 \int_0^t \frac{\partial g}{\partial \xi} \left[E_g g(\xi) + \int_0^\xi \frac{\partial E_{rel}(\xi-\tau)}{\partial(\xi-\tau)} g(\tau) d\tau \right] d\xi \right\} = 0 \quad (2.11)$$

where $u(t) = u_o g(t)$, the applied displacement

$$\begin{aligned} u_o &= \text{normalized radial boundary displacement} \\ E_g &= \text{glassy modulus} \\ E_{rel}(t) &= \text{relaxation modulus} \end{aligned}$$

For a step displacement imposed upon the spherical geometry, it is found that

$$\epsilon_{ocr}(a, t) = \sqrt{\frac{\gamma_c}{E_g a_o}} \quad (2.12)$$

or that the critical tangential strain at the flaw is independent of time as long as the surface energy density is constant.

For constant strain rate loadings, one finds that

$$\epsilon_{\theta_{cr}}(a, t) = \sqrt{\frac{\gamma_c}{2a_o \frac{E_{rel}^{(2)}(t_o)}{t_o^2}}} \quad (2.13)$$

where t_o - time to failure

$$E_{rel}^{(2)}(t_o) = \int_0^{t_o} \int_0^{\tau} E_{rel}(\xi) d\xi$$

It has been shown that⁽²⁰⁾

$$2 \frac{E_{rel}^{(2)}(t_o)}{t_o^2} \approx E_{rel}(t_o) \quad (2.14)$$

So then

$$\epsilon_{\theta_{cr}}(a, t) \approx \sqrt{\frac{\gamma_c}{a_o E_{rel}(t_o)}} \quad (2.15)$$

which, of course, reduces to the step load solution as $t_o \rightarrow 0$,

$E_{rel}(t_o) \rightarrow E_g$. Interestingly enough, the critical strain increases with time to an upper limit of $\sqrt{\frac{\gamma_c}{a_o E_r}}$. It is curious that, for the relation of critical strain to allowable mechanical properties suggested by Williams⁽¹⁹⁾ there is no allowance for subsequent decay for increasing time, unless the surface energy density is also a function of time, or unless there are peripheral changes (such as aging) that

cause E_r to increase.

Fracture kinetics may also be studied from this approach.

Setting the bracketed portion of equation (2.8) to zero yields the propagating flaw solution,⁽³⁷⁾ namely

$$a(t) = \left\{ \frac{2b^6}{T} \left(\frac{u_o}{b} \right)^2 \int_0^+ \frac{\partial g(\xi)}{\partial \xi} \left[E_g g(\xi) + \int_0^\xi \frac{E_{rel}(\xi-\tau)}{\partial(\xi-\tau)} g(\tau) d\tau \right] d\xi \right\}^{1/5} \quad (2.16 a)$$

or alternately

$$a(t) = \left\{ \frac{2b^6}{T} \left(\frac{u_o}{b} \right)^2 \int_0^+ \frac{\partial g(\xi)}{\partial \xi} \int_0^\xi \frac{\partial g(\tau)}{\partial \tau} E_{rel}(\xi-\tau) d\tau d\xi \right\}^{1/5} \quad (2.16 b)$$

Until the initiation of failure the flaw does not increase in size, i.e., $a(t) = a_o$ which means that the stationary flaw solution is satisfied. After initiation the flaw will increase in size. Provided the rate of flaw growth is small, the propagating solution equation (2.16 a) or (2.16 b) must be satisfied. At the point of initiation, however, both the stationary and the propagating solutions must be satisfied hence from equation (2.8), failure initiation occurs where

$$\frac{T}{2a_o} \left(\frac{a_o}{b} \right)^6 \left(\frac{b}{u_o} \right)^2 = \int_0^{+f} \frac{\partial g(\xi)}{\partial \xi} \int_0^\xi \frac{\partial g(\tau)}{\partial \tau} E_{rel}(\xi-\tau) d\tau d\xi \quad (2.17)$$

where $+f$ is the time to failure.

Evaluation of equation (2.17) for the simple loading functions can readily be done and some examples have been mentioned.

In most problems involving linear systems or materials the solution for the simple loading functions is all that is required. By the superposition principle the solution when the loading function is several simple loading functions applied simultaneously is simply the sum of the solutions taking each loading function individually. In most linear problems the response to an arbitrary loading function can be obtained from the response to a unit step function by application of the Duhamel Integral. In the formulation of the fracture problem, however, energy which is a function of the square of the loading function is involved so that these simplifying principles do not apply, hence it is necessary to consider these more complicated loading functions in greater detail.

2.2 LOADING FUNCTIONS WHICH ARE SUMS OF SIMPLE LOADING FUNCTIONS

Consider the situation where $g(t) = g_1(t) + g_2(t) + g_3(t) + \dots + g_n(t)$ Equation (2.17) then becomes

$$\frac{T}{2a_0} \left(\frac{a_0}{b} \right)^6 \left(\frac{b}{u_0} \right)^2 = \int_0^{t_f} \left[\sum_{i=1}^n \frac{\partial g_i}{\partial \xi} \int_0^{\xi} \left[\sum_{j=1}^n \frac{\partial g_j}{\partial \tau} E_{rel}(\xi - \tau) \right] d\tau \right] d\xi \quad (2.18)$$

Note that the solution includes the sum of the individual solutions considered separately and every possible combination of simple loading functions taken two at a time. Parenthetically, review of the equation predicts that the sequence of application of these simple loadings has no effect on the final result.

2.3 CYCLIC FATIGUE - SPHERICAL FLAW/CYLINDRICAL FLAW ANALYSIS

As an example of this general type loading, consider the case of sinusoidal loading with a superimposed preload which is suddenly applied. For this case

$$u(b,t) = u_o g(t) = u_p u(t) + u_o \sin \omega t \quad (2.19)$$

hence

$$g_1(t) = \frac{u_p}{u_o} u(t)$$

and

$$g_2(t) = \sin \omega t$$

It is further assumed that the Prony series representation for the relaxation modulus is adequate. Equation (2.17) may be evaluated to

$$\begin{aligned} \frac{T}{2a_o} \left(\frac{a_o}{b} \right)^6 \left(\frac{b}{u_o} \right)^2 &= \left(\frac{u_p}{u_o} \right)^2 E_g + \frac{u_p}{u_o} \sum_{i=1}^n \frac{\omega \tau_i}{1 + \omega^2 \tau_i^2} E_i + \frac{u_p}{u_o} E_e \sin \omega t_f \\ &+ \frac{u_p}{u_o} \sum_{i=1}^n \left(\frac{\omega \tau_i}{1 + \omega^2 \tau_i^2} \right) E_i e^{-t_f/\tau_i} (\omega \tau_i \sin \omega t_f - \cos \omega t_f) \\ &+ \frac{E_e}{4} (1 - \cos 2\omega t_f) + \sum_{i=1}^n \left(\frac{\omega \tau_i}{1 + \omega^2 \tau_i^2} \right) E_i \left[\frac{\omega t_f}{2} + \frac{\sin 2\omega t_f}{4} \right. \\ &\left. + \frac{\omega \tau_i}{1 + \omega^2 \tau_i^2} (e^{-t_f/\tau_i} \cos \omega t_f - 1) - \frac{\omega^2 \tau_i^2}{1 + \omega^2 \tau_i^2} (e^{-t_f/\tau_i} \sin \omega t_f) \right] \end{aligned} \quad (2.20)$$

It will be noted that the first term on the right side of equation (2.20), i.e., $(u_p/u_o)^2 E_g$, is simply the result for a suddenly applied constant displacement and the final two terms are those due to the sinusoidal loading leaving for the "cross terms."

$$\frac{u_p}{u_o} E_e \sin \omega t_f + \frac{u_p}{u_o} \sum_{i=1}^n \left(\frac{\omega \tau_i}{1 + \omega^2 \tau_i^2} \right) E_i \left[1 + e^{-t_f/\tau_i} (\omega \tau_i \sin \omega t_f - \cos \omega t_f) \right] \quad (2.21)$$

The results are illustrated in Figure 1, where equation (2.20) is plotted for both pure sinusoidal loading ($u_p = 0$) and sinusoidal superimposed upon a preload. It will be noted that failure will initiate in the sinusoidal-with-preload case before it will in the pure sinusoidal case. (21)

We can consider the response to a sinusoidal displacement for a three-element model and express the result in terms of the local strain at the internal flaw where N is the number of cycles to failure. One deduces easily, therefore, a characteristic fatigue curve behavior $|\epsilon_\phi(a)| = \frac{K(\omega)}{\sqrt{N}}$ showing the usual degradation of life, i.e., strain at failure, with an increasing number of cycles, but furthermore, that the proportionality factor distinct from metals--is frequency dependent.

In order to study this further, consider equation (2.20) with the cyclic terms removed, for a three-element model such that $E_1 = 9900$, $E_e = 100$, $E_1 = 1.0$ sec., $(u_p/u_o) = 1.0$, then

$$\frac{\gamma}{2a} \left(\frac{1}{\epsilon_{\phi}(a)} \right)^2 \approx 10,025 + 9,900 \frac{\omega}{1+\omega^2} + 9,900 \left(\frac{\omega^2}{1+\omega^2} \right) \left(\frac{1}{2} + \frac{1}{4} - \frac{1}{1+\omega^2} \right) \quad (2.22)$$

The general trend of allowable strain versus the number of cycles is shown for various frequencies in Figure 2. It is interesting to note that the number of cycles to failure (or fatigue life) is smallest at a frequency that corresponds to the peak of the low modulus curve, while at very low, or very high frequencies a much longer fatigue life is predicted. Equation (2.20) can be simplified for long times (so that the exponentials are negligibly small) and by substitution of the complex moduli for the Prony series. Rearranging it is then found that

$$\epsilon_{\theta}(a, t_f) = \frac{\sqrt{\frac{\gamma_c}{a_0}}}{\sqrt{\left(\frac{u_p}{u_0} \right)^2 E_g + E''(\omega) \left(\pi N + \frac{u_p}{u_0} \right) + \frac{\omega}{2} \frac{\partial E'(\omega)}{\partial \omega} + \dots}} \quad (2.23)$$

Further simplification can readily be made, and is shown in a parallel development for the cylindrical flaw.

Consider a plane-stress circular plate subject to displacement boundary conditions and having a cylindrical flaw in the center. Following the energy balance shown in Reference (19), it is found that⁽³⁸⁾ the equation representing the energy is

$$\dot{a} \left\{ \gamma - \frac{4}{3a^3(t)} \int_0^t \dot{S}(\xi) \left[S(\xi) E_g + \int_0^\xi \frac{\partial E_{rel}(\xi-\tau)}{\partial(\xi-\tau)} S(\tau) d\tau \right] d\xi \right. \\ \left. - 4a(t) \int_0^t \dot{P}(\xi) \left[P(\xi) E_g + \int_0^\xi \frac{\partial E_{rel}(\xi-\tau)}{\partial(\xi-\tau)} P(\tau) d\tau \right] d\xi \right\} = 0 \quad (2.24)$$

where

$$P(\xi) = \frac{g(\xi)}{2(1 - \alpha k^2)}$$

$$S(\xi) = -\frac{3}{2} \frac{g(\xi) \alpha a_o^2}{1 - \alpha k^2}$$

$$\alpha = \left(\frac{a(\xi)}{a_o} \right)^2$$

$$k = \frac{a_o}{b}$$

now letting $g(t) = u^*(t) + u_o \sin \omega t$, where $u^*(t)$ is a unit step function. The solution, assuming $a(t_c) = a_o$ at the time of fracture initiation, is as follows:

$$\frac{u_{ocr}}{b(1+3k^2)} = \frac{\sqrt{\gamma/a_o}}{2\sqrt{2}} \cdot \frac{1}{\sqrt{F(L,P,t)}} \quad (2.25 a)$$

where

$$\begin{aligned}
F(L, P, t) = & \left(\frac{u_p}{u_o} \right)^2 E_g + \frac{u_p}{u_o} E_e \sin \omega t + \frac{u_p}{u_o} \sum \left(\frac{\omega \tau_i}{1 + \omega^2 \tau_i^2} \right) E_i \left[1 + e^{-t/\tau_i} \right. \\
& \left. (\omega \tau_i \sin \omega t - \cos \omega t) \right] + \frac{E_e}{4} (1 - \cos 2 \omega t) \\
& + \sum E_i \left\{ \frac{\omega \tau_i}{1 + \omega^2 \tau_i^2} \left(\frac{\omega t}{2} + \frac{\sin 2 \omega t}{4} \right) \right. \\
& + \frac{\omega^2 \tau_i^2}{(1 + \omega^2 \tau_i^2)^2} \left(e^{-t/\tau_i} \cos \omega t - 1 \right) - \frac{\omega^3 \tau_i^3}{(1 + \omega^2 \tau_i^2)^2} \left(e^{-t/\tau_i} \sin \omega t \right) \\
& \left. + \frac{\omega^2 \tau_i^2}{4(1 + \omega^2 \tau_i^2)} (1 - \cos 2 \omega t) \right\} \quad (2.25 \text{ b})
\end{aligned}$$

which for relatively long times reduces to

$$\frac{u_{ocr}}{b(1+3k^2)} = \frac{1}{2\sqrt{2}} \sqrt{\frac{\sqrt{\gamma/a_o}}{\left(\left(\frac{u_p}{u_o} \right)^2 E_g + E''(\omega) \left(\pi N + \frac{u_p}{u_o} \right) + \frac{\omega}{2} \frac{\partial E'(\omega)}{\partial \omega} \right)}} \quad (2.26)$$

This relation has turned out to be, as expected, quite like that developed for the spherical flaw, differing only by the geometric constants.

Consider now the rearrangement of equation (2.26) for the purpose of more clearly defining the factors that influence the fatigue life, N , for a linearly viscoelastic material.

$$N = -\frac{u_p}{\pi u_o} + \frac{1}{\pi E''(\omega)} \frac{\gamma/a_o (b(1+3k^2))^2}{8 (u_{o_{crit}})^2} - \frac{\omega}{2} \frac{\partial E'(\omega)}{\partial \omega} - \left(\frac{u_p}{u_o}\right)^2 E_g \quad (2.27)$$

The only quantities that vary with frequency are $E''(\omega)$ and $\frac{\omega}{2} \frac{\partial E'(\omega)}{\partial \omega}$. The relation is simplified by recognizing $\frac{\omega}{2} \frac{\partial E'(\omega)}{\partial \omega}$ is small in comparison to E_g , then

$$N \approx A + \frac{B}{E''(\omega)} \quad (2.28)$$

thus for large values of E'' , the number of cycles to failure, N , will be small, or for small values of E'' then N becomes larger. And for $E'(\omega) \rightarrow 0$ (as for a perfectly elastic material) the number of cycles to failure is predicted to become infinite.

Such behavior has not been observed since perfectly elastic materials have not been observed. On the other hand, it has been observed that elasto-plastic materials have an increasing tendency to fatigue as they are loaded further into the plastic region. In an empirical study, Coffin⁽³⁹⁾ has shown that the relationship $N^{1/2} \Delta \epsilon_p = C$ fits the behavior for a wide variety of materials where $\Delta \epsilon_p$ is the plastic strain and C is a constant.

2.4 CYCLIC FATIGUE - CYLINDRICAL FLAW TESTS

2.4.1 Test Apparatus and Procedure

In order to experimentally verify the theoretical relations for the cylindrical flaw previously mentioned, a simple tension fatigue

test was used.⁽⁴⁰⁾ Scope of testing included demonstration of

- a) fatigue life dependence on frequency, and
- b) the influence of loading sequence.

A well characterized material, GALCIT I* was used in these tests. Particular care was exercised to prevent solvent and moisture exposure. Material stock and prepared samples were stored in dessicators until immediately prior to testing.

Individual specimens were cut to dimensions shown in Figure 3. Size and orientation of the flaw is highly critical. A slight variation from the established standard in flaw size, for example, would subsequently cause bad or erratic data scatter during tests.

A good deal of care was taken in making the initial flaw or crack uniform from specimen to specimen. A 1/32" hole was milled in the middle of each specimen to minimize tearing when the crack was cut into the specimen. The specimens were cut with a specially made, finely polished blade 0.0625 inches in width. Each specimen was placed in a holding fixture and the blade passed through the milled hole, perpendicular to the sides of the specimen. The flaw dimensions were chosen so that the stress intensity factor for a cracked plate could be used.⁽⁴¹⁾

2.4.1.1 Apparatus

The test machine viewed in Figure 4 was basically a slider crank mechanism driven by a 12 volt shunt wound DC motor. The field windings and armature were excited by separate regulated DC power supplies.

*50/50 mixture solithane 113 and castor oil, furnished courtesy Dr. R. Landel, California Institute of Technology.

The nature of the study required that the tests be run at two frequencies, consequently a third power supply was connected to be used interchangeably with the armature power supply. One was set at the lower frequency and the second was set at the higher frequency. The switching was accomplished with the application of a simple double pole, double throw switch. During frequency change and motor stabilization, only about 20 revolutions occurred. It was determined that 20 revolutions has essentially no effect and could be considered negligible when compared to total cycles required to reach failure in any of the tests being carried on.

Specimens were held by clamp type jaws as shown in Figure 4. Sandpaper was glued on the jaw faces to prevent slippage within the jaws which were made especially for the tests. The jaws were designed to hold firmly but not cause warpage or undue stress around the crack area.

As illustrated in Figure 4, the initial prestrain was applied by use on an adjustable eccentric on the top of the machine. The sinusoidal loading was developed through the crack which had a 0.05 inch offset. The resulting strain was as follows:

$$g(t) = u_p(u^*(t)) + .05 \sin \omega t$$

where $u^*(t)$ is a unit step function.

In all tests referred to in this work, u_p was set at 0.35".

Recognizing initial failure of the crack tip was critical to the study and difficult to accomplish. During the tests specimens were vibrated at frequencies ranging between 50 and 6,000 cycles per

minute. Initial failure was invisible to the naked eye. A strobe light was employed both to monitor the frequency and to serve as a light source focused on the crack. When the light was directed through the specimen at an angle of about 20° from the horizontal, the fracture surface appeared as a silvery line at the apex of the crack.

A microscope fitted with a special lens was used for detection of the initial failure. The special adaptation of the microscope made it possible to focus on the specimen from a point about two feet from the specimen during the test. The modified microscope provided magnification approximating 20x.

The combined use of the strobe light and the microscope made it possible to see the fracture before it had grown beyond 0.001 inch, which was considered satisfactory for the purposes of the study. Figure 5 illustrates the relative position of the strobe, the specimen, and the microscope.

The number of cycles the specimen had been subjected to was recorded on an Altec digital counter. Reliable triggering was obtained by use of a photoresistor, and a mirror attached to the rotating motor shaft.

2.4.1.2 Procedure

A specimen to be tested first had a crack precut in it. It was next mounted in the test device and run at constant frequency until failure. After fracture initiation, flaw size was monitored. Characteristic flaw growth rate data are shown in Figure 6. For the dual frequency or sequential test the specimen was run at one frequency for approximately half the previously estimated failure time

at that frequency. The motor was then switched to the second power supply for the other frequency until failure was noted.

Three specimen were tested in one sequence and then an additional three were tested with the order of the frequencies reversed. The samples were numbered and the crack growth that occurred was measured.

When a specimen is being fractured, any interruption in the fracture growth will cause a line or leave-off mark to appear across the fracture surface. It was found that when the specimens were quickly pulled or jerked apart, the leave-off mark was clearly discernible. Test crack growth was measured under a 40x microscope and recorded. The results are shown in Tables 2 and 3.

Temperature increases were detected during this series of tests and subsequent tests were instrumented in an attempt to accurately measure those temperatures at the apex of the crack.

A thermistor was used to measure the temperature change anticipated to be in the 80° to 120°F range. A thermistor with 0.001 inch leads and a 0.007 inch uncovered bead was potted onto the surface near the apex of the crack with Solithane. After the Solithane had polymerized, the sample was tested and the output of the thermistor monitored. This procedure gave very good results as shown in Figure 7.

The analytical description of this heating problem is complicated. However, by making simplifying assumptions, a qualitative description of the temperature rise may be given and the complexity of the problem illustrated.

2.4.2 Heat Transfer Analysis

Let us consider an infinite sheet of linearly viscoelastic material subjected to strain cycling at a frequency ω . It is found that using the complex modulus representation $E^*(\omega) = E'(\omega) + iE''(\omega)$ where $\epsilon = \epsilon_0 e^{i\omega t}$;

$$u''' = \frac{\omega}{2} E''(\omega) \epsilon_0^2 \quad (2.29)$$

where $u''' =$ energy dissipation density per unit time

$E''(\omega) =$ "loss modulus"

$\epsilon_0 =$ strain half amplitude

Now suppose that the sheet of material, infinite in length and width, but of thickness, $2L$, is cooled by convective heat transfer on the faces $|x| = L$ (where x is measured from the midplane of the sheet). Then it is a matter of setting up an energy balance or

$$\text{Heat dissipated} = \text{Heat stored} - \text{Heat transferred} \quad (2.30)$$

Differentiation of the energy balance with time and rearranging gives

$$\frac{d}{dt} \int_0^L \rho C T dx = u''' L = -q_n = -\kappa \left. \frac{\partial T}{\partial x} \right|_{x=L} \quad (2.31)$$

where $\rho =$ material density

$C =$ specific heat

$\kappa =$ thermal conductivity

$q_n =$ rate of convective heat transfer

If the energy dissipation rate, u''' , were independent of temperature, T , and space, x , the equation is linear and is easily solved. However, u''' is proportional to the loss modulus and the square of the imposed strain. For linear viscoelastic materials the loss modulus in turn is temperature (and thus space) dependent and the strain can also in particular problems be space and temperature dependent. When each of these terms is fully developed and of such magnitude so that they are not negligible, coupling exists between the heat transfer equations and the stress/strain field equations. The term thermo-mechanical coupling is then applicable.

For the time being, however, let us assume, somewhat artificially, that the energy dissipation rate, u''' is independent of temperature and space. Then the solution for equation (2.31) is⁽⁴²⁾

$$\frac{T(x,t) - T_{\infty}}{u''' L^2/\kappa} = \frac{1}{2} \left[1 - \frac{x^2}{L^2} + \frac{2\kappa}{hL} \right] \left[1 - e^{-\frac{3h + \frac{hL}{\kappa}}{\rho CL(\frac{hL}{\kappa} + 3)}t} \right] \quad (2.32)$$

where h = convective film coefficient

T_{∞} = initial sample and environmental temperature

or rearranging

$$T(x,t) - T_{\infty} = \left[\frac{\omega}{4} \frac{L^2}{\kappa} E''(\omega) \epsilon_o^2 \right] \left[1 - \frac{x^2}{L^2} + \frac{2\kappa}{hL} \right] \left[1 - e^{-t/\tau_1} \right] \quad (2.33)$$

where $\tau_1 = \frac{\rho CL(\frac{hL}{\kappa} + 3)}{3h}$

The first bracketed term on the right hand side of equation (2.33) indicates the magnitude of the temperature rise to be proportional to the loss modulus and the square of the imposed strain. The second bracketed term shows the temperature distribution through the thickness of the sheet to be parabolic. But for thin sheets or where $\frac{2\kappa}{hL} \gg 1 - \frac{x^2}{L^2}$, the temperature may be considered constant through the sheet. In the experimental tests previously described, $L = 0.05$ in., $\kappa = 1.5$ Btu in./hr ft² °F and $h \approx 1.0$ Btu/hr ft² °F and $2\kappa/hL \approx 60$ thus the temperature gradient is negligible.

Then from the last term, the term τ_1 is identified as the time constant, and indicates the rapidity with which the temperature rises. For very long times, i.e., steady state, this term is unity.

Thus, for application to the simple tension fatigue test, inasmuch as the one dimensional-constant heat dissipation rate assumptions are valid, the expected sample temperature could be approximated by

$$T(t) = T_{\infty} + \frac{\omega}{4} \frac{L^2}{\kappa} E''(\omega) \epsilon_0^2 \left[1 - e^{-t/\tau_1} \right] \quad (2.34)$$

Now it is appropriate to re-examine the assumptions regarding the energy dissipation rate. Fortunately, for the particular case at hand, the temperature variation through the thickness is negligibly small, then it is concluded that the strain is independent of space (i.e., $\frac{d\epsilon}{dx} = \frac{d\epsilon}{dT} \frac{dT}{dx} = 0$). However, the influence of temperature is not so easily disposable. The variations of $E''(\omega)$ with temperature may be seen by reviewing the variations of $\log a_T$ versus temperature (Figure 8) and then associating ω with ωa_T . Loss modulus

versus ωa_T data for GALCIT I are shown in Figure 9.⁽⁴³⁾

The effect of a temperature increase is to slide the curve to the right. Thus, for frequencies left of the curve peak, increases in temperature effect a reduction in $E''(\omega a_T)$. The estimated result is reflected in comparison with predicted values, using constant loss modulus in Figure 10. It is noted that the equilibrium temperature is less than that predicted using the initial, but constant value for $E''(\omega)$.

But if, on the other hand, an excitation frequency greater than that corresponding to the curve peak were imposed, the result is estimated to be quite different. The loss modulus versus frequency curve again shifts to the right with increasing temperature, but the effect is now to increase the loss modulus. Then the resulting sheet temperatures would be greater than those predicted using the initial loss modulus value.

Now examine the effect of the variation of $E''(\omega)$ with temperature on fatigue life. From the cylindrical flaw model, it was noted that

$$N_f \approx A + \frac{B}{E''(\omega)} \quad (2.28)$$

But now, due to the manner in which $E''(\omega)$ varies with ω , fatigue life (N_f) may be estimated versus ω as shown in Figure 11.

If constant frequencies left of the valley in the curve are imposed, increasing temperatures again slide the curve to the right, and the predicted fatigue life may be visualized as a magnetic bead that remains at the intersection of the sliding curve and the vertical

line corresponding to the imposed frequency. Then $N_{f \text{ heated}} > N_{f \text{ isothermal}}$. Using again the same analogy on the right hand portion of the curve, it is estimated that $N_{f \text{ heated}} < N_{f \text{ isothermal}}$.

Before getting too far afield with these descriptions, let us go back and critically review what has been done. First of all, the coupling between $E''(\omega)$ and temperature has not been properly incorporated into the energy balance relations for the transient heating problem, nor for the fracture criticality conditions. Secondly, fracture criticality predictions were made assuming the surface work term independent of temperature and time. This assumption is also suspect, and will be discussed later.

Thus at the most, the foregoing discussion must be qualitative with the accuracy of reasoning to be assessed upon examination of experimental test results.

2.4.3 Discussion of Data

To demonstrate that the fatigue life for this viscoelastic material is frequency dependent, constant frequency tests were run at several frequencies. The resulting data are shown in Table 2.

It is noted that the number of cycles to failure increases with the test frequency; but since the loss modulus monotonically increases with frequency in the range of test frequency imposed (Figure 9), the analytically predicted fatigue life (equation (2.28)) diminishes with increasing frequency. Although fatigue life of viscoelastic material is frequency dependent, in these simple tests

this dependence is masked by the sample temperature rise. Just to check this out, air from an electric fan was directed on some additional samples during test to promote convective cooling and these samples failed at slightly lower number of cycles. These data points are indicated by Δ 's in Figure 12. Temperature changes resulting from the viscous energy dissipation are important and analytical predictions concerning fatigue life will be incorrect if these changes are neglected. Temperatures were measured on subsequent test samples. Samples tested at 500 cpm experienced temperature change from 70°F at the beginning of the test to 76°F at fracture. At a frequency of 1000 cpm the temperature rose to 78.5°F and at a frequency of 5000 cpm the temperature rose to 98°F. These measurements were somewhat erratic since the thermisters used to measure the temperature were not always placed over the hottest spot, which incidentally was not at the apex of the crack.

Dual-frequency tests were run to investigate the analytical prediction that reversing the sequence of loading does not affect the fatigue life. The test data are shown in Table 4. The extreme right hand column of Table 4 shows the percentage difference in fatigue life accuracy as a result of reversing the order or the sequence of loading. The positive difference in this column indicates the failure occurred in fewer total cycles in tests where the higher frequency was applied first in the testing sequence. A percentage difference of zero would indicate no effect attributable to loading sequence. A negative percentage difference would have indicated the reverse of what the tests showed. If the assumption of isothermal testing were

valid, these results would be contrary to the fatigue theory previously developed. However, the temperature does change and the manner of change depends on loading sequence. This is graphically illustrated by Figure 6. These results show markedly more rapid temperature increase at higher frequencies than at lower frequencies. This is in basic agreement with the simple heat transfer analysis previously described. The qualitative assessment of the heating effects also appears valid since $N_{f \text{ heated}} > N_{f \text{ isothermal}}$. Note is also made that a good approximation to the heat transfer equations can be made using numerical techniques. By iteratively readjusting the loss modulus with temperature (equation 2.34) for long times through use of the frequency-temperature shift factor, equilibrium temperatures in an infinite sheet can be approximated. This would be important to the quantitative evaluation of these tests; however, it is considered beyond the scope of this study for the following reasons.

First, because of the crack, a non-uniform strain distribution exists that give rise to a special dependent temperature and thus modulus. The departure from homogeneity makes this a thermomechanically coupled problem, complex in its own right and worthy of a separate study.

Secondly, temperatures at the apex of the crack would seem to be very important. Brief infrared examination of a fatiguing specimen shows the area immediately adjacent the crack apex to be cooler than most of the rest of the specimen. This seems due to the opening and closing of the crack under cyclic loading, rapidly pumping of air in

out, which locally cools the crack surfaces. The thermal field equations in the neighborhood of the crack tip can then no longer be considered one dimensional (through the thickness), thus further complicating the problem.

These features are included in recommendations for further study.

2.4.4 Fracture Surface Examinations

The fracture surfaces, resulting from the cyclic fatigue of the GALCIT I specimen previously described, were examined using optical and electron microscopes. Some of the techniques used for examination and the more significant features observed will be briefly discussed.

The rubber fracture surfaces displayed many features similar to those observed from metal fracture surfaces, hence, much of the terminology and nomenclature used by metallurgists will be adopted.

Optical microscopic examination was conducted for a large number of fatigue fractured specimen, both using transmitted and reflected light. Transmitted light showed more surface definition. Various colored filters were also tried, but were not effective in enhancing contrast of the surface features. Magnifications between 50x and 200x showed a moderate amount of detail. At magnifications above 200x the fracture surface was so irregular, large portions of the field of view were out of focus. Therefore, most of the examinations were performed at the lower magnifications.

One of the most characteristic features of the fatigue fracture surfaces was the striped or striated appearance (shown in Figure 13). The lines appeared perpendicular to the direction of progressive flaw

extension. The spacing between these lines was very small near the original flaw and became progressively larger as the flaw size increased. The spacing also changed with the frequency of testing; small spacing corresponded to high frequencies and larger spacing corresponded to lower frequencies. Interrupted cyclic tests and dual frequency tests demonstrated a one to one correspondence between the number of cycles imposed and the number of striations observed. The growth history of the flaw appeared to be start-stop by nature, and at each new start a tell-tale line or striation was left as a record of the fracture front location. The flaw growth for each cycle can easily be determined by direct measurement of the distances between the striations. The influence of frequency on the spacing between striations is shown in Figure 14. A cyclic displacement was imposed at a frequency of 90 cpm, then quickly the frequency of this displacement was increased to 280 cpm also for 50 cycles, and so on. The photograph (Figure 14) was taken intentionally slightly out of focus to show the gross effect of the dual-frequencies imposed. Readjustment of the focus shows the 50 striations within each of the broad bands.

It is also noted from Figure 1 that the fracture surface did not progress along the same plane, but rather on a "split level". The junctures between these different levels was approximately parallel to the direction of fracture propagation and are called river markings. Frequently these river markings join so the step between levels of the fracture surface is greater. These different levels seem to stem from the cut surface of the original flaw and special

care was taken to make the original flaw cut uniform such that all fracture progressed on the same plane, but this was not accomplished.

A small area of the fracture surface near the initial flaw was examined using a transmission electron microscope. A two-stage carbon replica was made of the fracture surface using acetate tape softened by acetone, then by vapor-depositing carbon and then shadowing with germanium. This technique leaves much to be desired since the acetone swells the GALCIT I sample. A photograph of the replica taken at 13,500x is shown in Figure 15 and the poor quality of the replica is noted. However, the dark lines corresponding to the fatigue striations can be seen. Carbon collapse along these lines indicate a large step between adjacent planes. There also appears to be a faint line midway between the striations, but perhaps too much credence should not be placed in the replica.

Several other replicating techniques were unsuccessfully attempted. It appeared a more efficacious approach was direct examination of the surfaces using a scanning electron microscope.

Sample preparation for the scanning electron microscope involves vapor depositing a thin (100\AA)⁶ gold coating over the specimen and introducing it directly into the microscope.

Two specimen were examined with the scanning microscope. One specimen of GALCIT I was fractured in simple tension. The fracture surface, shown in Figure 16, clearly shows the river markings. Curiously, however, the ribbed appearing river markings are almost perpendicular to the gross over-all direction of fracture propagation

indicating local fracture front propagations quite different from the gross fracture front movement. Such local perturbations introduce errors in gross fracture predictions. This appears to be a fruitful area for further investigation.

The second specimen examined, shown in Figure 17, was loaded by cyclic displacement for 1000 cycles at a frequency of 3000 cpm. This specimen was fabricated and tested as the other fatigue specimen, except that for the number of cycles imposed, fracture should not have initiated. Other investigators of fatigue have postulated that fracture initiates on the first cycle and propagates such a small distance on that and subsequent cycles that it is frequently unnoticed until it has propagated a macroscopically measurable distance. The corresponding number of cycles is then denoted as the fatigue life for the particular imposed strain level. It is easy to envision that the flaw may grow a certain distance before its extension is visually detected, but not so readily apparent, in view of the analytical predictions, that the fracture initiation occurs on the very first cycle. So this specimen was loaded to over 90% of its expected fatigue life, removed from the fatigue apparatus, manually pulled apart, then examined. The photograph shown in Figure 17 illustrates the river markings tear lines characteristic of the manual tensile fracture, but does not portray any features of fatigue fracture. Admittedly, repeated examination can be made at higher magnifications for additional specimen with accumulated cycles progressively nearer their fatigue life until finally fatigue fracture features are observed. Perhaps a more direct approach would be to fatigue a specimen

until failure is visually detected, then go back and count the fatigue striation and subtract from the total cycles accumulated. This technique, incidentally, was attempted using the optical microscope, but definition at high magnification was not adequate for quantitative work.

III. ADHESION

3.1 ANALYTICAL DEVELOPMENTS

It has been previously introduced that cohesive and adhesive fracture are similar and a simple pressurized blister configuration has been suggested for evaluation of adhesive bonds. However, it is recalled that it was assumed that an incompressible material was bonded to a rigid material. It is now appropriate to inquire what will be the effect of departing from these assumptions.

From Malyshev and Salganik⁽³³⁾ the stress distributions near a crack for a bond line subjected to tension and shear is:

$$\sigma_y = \frac{-1}{\sqrt{r}} (A_0 \cos (\beta \ln \frac{r}{a+r}) - B_0 \sin (\beta \ln \frac{r}{a+r}) + O(1)) \quad (3.1)$$

$$\tau_{xy} = \frac{-1}{\sqrt{r}} (A_0 \sin (\beta \ln \frac{r}{a+r}) + B_0 \cos (\beta \ln \frac{r}{a+r}) + O(1)) \quad (3.2)$$

where

$$\beta = \frac{1}{2\pi} \ln \left[\frac{G_1 + G_2(3-4\nu_1)}{G_2 + G_1(3-4\nu_2)} \right] \quad (3.3)$$

and where A_0 and B_0 are stress intensity factors, β is the distance from the crack tip along the interface, a is the crack half length, and G , ν are the shear modulus and Poisson's ratio, respectively. For similar materials above and below the bond line, it is apparent that $\beta = 0$, and the stresses are proportional to $r^{-1/2}$. And, of course, when $\nu_1 = 0.5$ and G_2 or E_2 approach ∞ , $\beta = 0$ again. When the

materials are different ($\beta \neq 0$), the relations remain qualitatively the same at a distance from the crack tip exceeding x^* ; where

$$x^* \approx a e^{-\pi/2\beta} \quad (3.4)$$

At smaller distances, ($r < x^*$) the relations change; stresses infinitely growing in amplitude with infinitely increasing frequency as one approaches the crack tip. The difficulty seems to lie in the mathematical model as one has difficulty imagining the physical effect on continuity. The fault can be corrected by consideration of the contact stresses on an assumed convex shape being pressed together in the region of stress oscillations. None the less, these corrections need not be made as long as β is very small. Consider, for example, a bond interface between a rubber, $E = 400$ psi, $\nu = 0.5$ and glass $E = 10^7$ psi, $\nu = 0.25$ then β is calculated to be of the order of 10^{-6} .

Since β is so small and corrections need be only applied over a small region, $x^* \approx a e^{-10^6}$, the solution can be approximated by neglecting these corrections and we can proceed as Williams⁽²¹⁾ suggested.

Consider a disk of rubber bonded to a glass disk, with a small circular unbond of radius R into which a gas pressure may be introduced (see Figure 18).

By considering the upper sheet to be a plate with small deflections, fixed at the edges, from plate bending theory⁽⁴⁴⁾ it is found that

$$w(r) = \frac{PR^4}{64D} \left(1 - \left(\frac{r}{R}\right)^2\right)^2 \quad (3.5)$$

where

$$D = \frac{Eh^3}{12(1-\nu^2)} = \frac{Eh^3}{9}$$

An energy balance gives

$$\dot{I} = \dot{F} + 2D + \dot{SE} \quad (3.6)$$

where

$$\begin{aligned} \dot{I} &= \text{energy input} \\ \dot{F} &= \text{energy stored} \\ 2D &= \text{energy dissipation rate} \\ \dot{SE} &= \text{surface energy} \end{aligned}$$

and the dot indicates differentiation with respect to time.

But for an elastic material (zero energy dissipation) and taking the variation with respect to fracture surface area, the energy rate balance reduces to

$$\delta(U - A)_{eq} = 2\pi R \gamma_a \quad (3.7)$$

where

$$A_{eq} = \int_0^{Area} Pw(r) \, d \text{Area} \quad (3.8)$$

Some effort can be saved here by recognizing that for this

linear system, Clapyron's Theorem gives $U_{eq} = \frac{1}{2} A_{eq}$. Then making the energy balance it is found that the critical pressure (necessary to initiate debonding) is

$$P_{cr} = \left(\frac{32}{3(1-\nu^2)} \left(\frac{h}{R} \right)^3 \right)^{1/2} \sqrt{\frac{E\gamma_a}{R}} \quad (3.9)$$

or rearranging

$$P_{cr} w_o = 2 \gamma_a \quad (3.10)$$

It is recognized that the plate equations are applicable as long as the deflections are small and bending considerations are of primary importance. It is also recognized that as the deflections become larger, midplane stretching of the bonded specimens, or membrane stresses grow until finally they overshadow the bending contribution and predominate. It is clear that fracture criticality description may be bounded on the one hand for small deflections by using plate analysis and on the other hand for large deflections by using membrane analysis. It turns out this is a relatively simple task.

Membrane analysis, where deflection is assumed of the form⁽⁴⁴⁾

$$w(r) = w_o \left(1 - \frac{r^2}{R^2} \right)^2 \quad (3.11)$$

and for an incompressible linearly elastic material

$$w_o = 0.652 R \sqrt[3]{\frac{pR}{Dh}} \quad (3.12)$$

then energy balance considerations^{**} give⁽⁴⁵⁾

^{**}Note: For the membrane that $w_o = k(p)^{1/3}$. It can be shown that where $w = a p^{1/n}$ the strain energy at equilibrium is equal to $1/n+1$ times the applied work at equilibrium. Then $U_{eq} = 1/4 A_{eq}$ in this situation and the energy balance becomes $\delta(-3A_{eq}) = 2\pi R\gamma_a$ where

$$A_{eq} = \int_0^{Area} P[w(r)] d/Area .$$

$$p_{cr} w_o = 2.4 \gamma_a \quad (3.13)$$

For an analysis where the contribution of both plate bending and membrane stresses, the derivation is somewhat more complicated. The solution has been approximated by Berger,⁽⁴⁶⁾ who reduces the two field equations in the in-plane deformation, $u(r)$, and bending deflection, $w(r)$, to only one equation where a relation for evaluation of a nonlinear term in that equation is derived from considering the displacement boundary condition $u(R) = 0$.

Consider the strain energy relation for an axisymmetric plate shown in Figure 18. This relation can be simplified by recognizing that the contribution of the second strain invariant, e_2 , is negligible in comparison to the other terms.

$$U = \pi D \int_0^R \left\{ (\nabla^2 w)^2 + \frac{12}{h^2} e_2^2 - 2(1-\nu) \left[\frac{12}{h^2} e_2 + \frac{1}{r} \frac{\partial w}{\partial r} \frac{\partial^2 w}{\partial r^2} \right] \right\} r dr \quad (3.14)$$

From the application of the principle of virtual work, the field equation is found to be

$$\nabla^4 w - \alpha^2 \nabla^2 w = -\frac{P}{D} \quad (3.15)$$

where

$$\alpha^2 \equiv \frac{\alpha^2 h^2}{12} \quad (3.16)$$

The α term is determined using the boundary condition on the radial deflection u , i.e.

$$\left(\frac{PR^4}{Dh}\right)^2 = \frac{\frac{1}{3}(\alpha R)^6}{\frac{3}{4} + \frac{4}{(\alpha R)^2} - \frac{I_0(\alpha R)}{(\alpha R)I_1(\alpha R)} - \frac{1}{2} \frac{I_0(\alpha R)^2}{I_1(\alpha R)}} \quad (3.17)$$

where $I_0(\alpha R)$ and $I_1(\alpha R)$ are modified Bessel functions of the zero and first order, respectively.

Using the above equations, the deflection is calculated to be

$$w(r) = \frac{PR^2}{4D\alpha^2} \left[1 - \left(\frac{r}{R}\right)^2 - \frac{2}{\alpha R} \left(\frac{I_0(\alpha R) - I_0(\alpha r)}{I_1(\alpha R)} \right) \right] \quad (3.18)$$

For a circularly symmetric incompressible plate, fixed at the edges and loaded with a uniformly distributed load, P , equation (3.14) becomes

$$U = \pi D \int_0^R \left(r \left(\frac{\partial^2 w}{\partial r^2} \right)^2 + \left(\frac{\partial w}{\partial r} \right) \left(\frac{\partial^2 w}{\partial r^2} \right) + \frac{1}{r} \left(\frac{\partial w}{\partial r} \right)^2 + \frac{\alpha^4 h^2}{12} r \right) dr \quad (3.19)$$

Now applying the energy balance, but taking variations with respect to the variable αR ,

$$\frac{\partial}{\partial(\alpha R)} [U - A]_{eq} = 2\pi R \gamma_a \cdot \frac{\partial R}{\partial(\alpha R)} \quad (3.20)$$

where $\frac{\partial R}{\partial(\alpha R)}$ is determined from equation (4.17)

$$\frac{\partial R}{\partial(\alpha R)} = \frac{2\left(\frac{Dh}{P}\right)^2 (\alpha R)^5 - R^8 \left[\left(\frac{I_0(\alpha R)}{I_1(\alpha R)} \right)^3 - \frac{8}{(\alpha R)^3} - \frac{1}{\alpha R} - \frac{I_0(\alpha R)}{I_1(\alpha R)} \right]}{8R^7 \left[\frac{3}{4} + \frac{4}{(\alpha R)^2} - \frac{1}{\alpha R} \frac{I_0(\alpha R)}{I_1(\alpha R)} - \frac{1}{2} \left(\frac{I_0(\alpha R)}{I_1(\alpha R)} \right)^2 \right]} \quad (3.21)$$

Using equations (3.18) and (3.19) and developing the relation for "applied work"

$$(U-A)_{eq} = 2\pi \frac{P^2 R^2}{8D\alpha^4} \left[\left(\frac{l_o}{l_l} \right)^2 \left(\frac{(\alpha R)^2}{2} - 1 \right) - (\alpha R)^2 - 4 - \alpha R \frac{l_o}{l_l} + \frac{1}{l_l^2} + \frac{\alpha^8 h^2 D^2}{6P^2} \right] \quad (3.22)$$

where equation (3.8) gives

$$A_{eq} = 2\pi \int_0^R Pw(r) r dr$$

After the variation of equation (3.22) is taken with respect to αR , the surface energy density can be evaluated to be

$$\begin{aligned} \gamma_a = & -\frac{P^2}{8D} \left\{ \frac{R^5}{\frac{\partial R}{\partial(\alpha R)}} \left[\frac{l_o}{l_l} \left(\frac{1}{(\alpha R)^2} - \frac{4}{(\alpha R)^4} - \frac{1}{(\alpha R)^4 l_l} \right) + \left(\frac{l_o}{l_l} \right)^3 \left(\frac{2}{(\alpha R)^4} - \frac{1}{(\alpha R)^2} \right) \right. \right. \\ & + \left. \left(\frac{l_o}{l_l} \right)^2 \left(\frac{2}{(\alpha R)^5} - \frac{1}{(\alpha R)^3} \right) + \frac{1}{(\alpha R)^5} \left(\frac{1}{l_l} - \frac{4}{l_l^2} \right) + \frac{3}{(\alpha R)^3} + \frac{16}{(\alpha R)^5} \right] \\ & + 6R^4 \left[\left(\frac{l_o}{l_l} \right)^2 \left(\frac{1}{2(\alpha R)^2} - \frac{1}{(\alpha R)^4} \right) - \frac{1}{(\alpha R)^2} - \frac{4}{(\alpha R)^4} + \frac{l_o}{(\alpha R)^3 l_l} + \frac{1}{(\alpha R)^4 l_l^2} \right] \left. \right\} \\ & - \frac{Dh^2}{24} \left[\frac{2\alpha^3}{\frac{\partial R}{\partial(\alpha R)}} - \alpha^4 \right] \quad (3.23) \end{aligned}$$

This relation is not easily evaluated, thus has been programmed for evaluation on the computer. It should be noted from equations (3.21), (3.22), and (3.23) that the variables h and R appear with

exponentials as high as 8. Thus any error in measurement of these variables will strongly affect the result, depending also on their magnitude.

The bonded plate geometry readily lends itself to experimental verification of the continuum interpretation of adhesion concept. To review for a moment the predicted response, recall the elastic plate equation is (see equation (3.9))

$$w_o = \frac{R^4}{64D} P \quad \text{where} \quad D = \frac{Eh^3}{12(1-\nu^2)}$$

or

$$w_o = K P$$

Stability of the plate may be investigated by recalling criticality is defined when

$$\begin{aligned} \frac{d}{dR} (U - SE) &= 0 && \text{Criticality} && (3.25) \\ &< 0 && \text{No fracture} \\ &> 0 && \text{Accelerating fracture and kinetic energy terms} \\ &&& \text{must be added when velocity significant.} \end{aligned}$$

$$\frac{d}{dR} (U - SE) = \frac{P^2 R^5}{64D} - 2\pi R \gamma_a \quad (3.26)$$

Note that the rate of strain energy release is proportional to R^5 whereas the surface energy rate is linear with R .

In order to maintain criticality, then

$$\frac{P_{cr} R^4}{(2\pi)64D} - \gamma_a = 0 \quad (3.27)$$

and

$$P_{cr} = \frac{2\pi(64)D\gamma_a}{R^4} \quad (3.28)$$

From these relations, it is easily seen that a constant applied pressure gives rise to unstable or accelerating fracture.

For the pressurized plate, the central deflection is linearly proportional to the pressure as long as the radius of unbond (R) does not change; but when adhesive fracture takes place, then R increases and the deflection can possibly increase with no further increase in pressure. Consider now what happens when the pressure is reduced. The deflection may continue to increase with decrease in pressure until fracture decelerates and stops, then R , which is equal to $R + \Delta R$ (where ΔR is the distance of fracture propagation) remains constant with further reduction in pressure and again deflection is linearly proportional to pressure. This procedure may be repeated if the rates of fracture propagation are small. Recall that the locus of criticality conditions is a hyperbola in the pressure versus deflection diagram of parametric value $2\gamma_a$ for the region of small deflections. For large deflections, the parametric value of the hyperbola is $2.4\gamma_a$. Also, for the large deflection region, the membrane equations are applicable and one expects that

$$w_o = k_2 \left(\frac{P}{k_3} \right)^{1/3} \quad (3.29)$$

As long as p/k_3 is less than unity, the pressure versus deflection curve, excluding fracture will have positive curvature, i.e., will tilt upward. Then as p/k_3 becomes greater than unity, the curvature becomes negative. Fracture, and associated increases in the unbond radius also reduce the curvature toward negative values, thus fracture would be difficult to deduce from pressure versus deflection diagrams in the membrane region.

Fracture data points would be expected to lie on their respective hyperbolas in the small deflection and large deflection regions, and to be distributed in an orderly manner in between in the mixed bending and membrane region.

3.2 BLISTER PEEL TESTS

Bonded plate specimens were prepared by casting liquid polyurethane*** onto prepared glass and metal circular plates.⁽⁴⁷⁾ A small hole had been drilled in the center of each plate and fitted with a plugged pressure fitting so that the surface onto which the rubber was cast was flat. Lens quality polished glass plates were used and the metal plates had been surface ground but not polished. The surfaces were solvent cleaned prior to casting. The cast specimen were then cured. Following cure, the plug was removed from the pressure fitting and regulated air supply and pressure transducer were attached. An LVDT (Linear Variable Differential Transformer) was mounted in a

*** 50/50 mixture of Solithane 113 and catalyst purchased from Thiokol Chemical Company.

tripod arrangement above the specimen to measure central deflections. Electrical connections were made from the pressure transducer and LVDT to an X-Y recorder so that real time pressure versus deflection were directly plotted. Test apparatus and specimen are shown in Figures 19a and 19b.

Air pressure was then carefully introduced into the specimen causing the rubber to blister up and then peel away from the plates. Hence developed the blister peel test. Initial fracture was induced by air pressure to eliminate the effects of flashing around the pressure fitting. Initiation was detected visually using a telemicroscope. An air flow constriction was placed in the supply line so that the unbond progressed relatively slowly and fracture propagation could be interrupted by reducing the pressure. As a result multiple tests could be run on each specimen. Shown in Figure 20 are results from a rubber/glass specimen. Fracture initiation points are shown in Figure 21. It is recalled from equation (3.10) that the locus of fracture points would fall along a hyperbola of parametric value of $2\gamma_a$ from a plate theory. Indeed, while the deflections are small, the data points seem to follow this curve.

Note also that the γ_a value is determined from this curve, so at least one data point would coincide anyway. Then where the deflections became large, the fracture points should tend toward a hyperbola of parametric value $2.4\gamma_a$. This is due to the midplane stretching or membrane stresses in the rubber specimen becoming more significant until finally they predominate and the membrane solution is applicable.⁽⁴⁵⁾ In the transition between the bounding curves,

γ_a is determined using equations (3.21) and (3.23) where α is determined from equation (3.17). For a number of specimen prepared in the same manner and tested under similar conditions, it appears γ_a between polyurethane and glass is about 0.22 in #/in². Duration of each test was about two minutes. For similar time lapses, values for the cohesive surface energy for this material was found to be about 1.4 in#/in². Adhesive surface energies less than cohesive values are expected since breaking primary bonds involved in cohesive fracture requires more energy than the secondary bonds of adhesion and because of surface contamination in adhesion.

3.2.1 *Experimental Observations*

A number of other tests were run, not primarily to verify the continuum approach to adhesion, but rather to explore the implications of some unusual observations. Since these are of peripheral interest, the results will only be briefly described.

Problems were encountered in deflating the blister, and then reinflating because the rubber almost invariably restuck to the substrate. Calculated "fracture energy" values were erratic and ranged between 0.5 and 0.9 of the original value. The nature of the original bond and also the resticking was concluded to be of the Van der Waals type; but it is hypothesized that small pockets of air (microscopic or smaller) were entrapped during the resticking so that subsequent fracture passed through the now existing voids and are interpretable only with a knowledge of the size and distribution of these voids. The fracture is visualized to progress

along a spongy interface. It may be that the original bond interface is similar in nature, but with less frequently occurring flaws. If such is the case, experimental values of the fracture energy will be lower than values predicted on a molecular basis. However, regardless of what is happening micro or submicro-scopically, the test results are valuable for an engineering evaluation of the bond integrity.

One of the purposes for deflating and reinflating the blister was to determine the viscoelastic effects, if any. The resticking, previously mentioned, made the response at first glance appear viscoelastic. However, when powdered talc was injected into the air supply hole, the resticking was partially prevented and the pressure versus deflection curves for deflation were more closely approximated by the reinflation curves. Tests were also run in which the pressure was increased linear with time until about 0.9 of the pressure necessary to cause fracture and then held. Deflection increases occurring at this constant pressure were generally associated with flaw size increases as visually detected (using telemicroscope). Deflection increases were sometimes measured without observed flaw size increases, but the observer could not monitor the entire periphery of the blister. Stress relaxation would affect an increase in deflection at constant pressure and constant flaw size. The viscoelastic effects present were small since the tests were run slowly in comparison to the relaxation time for the material and were obscured by the resticking effects.

Another feature of the test results was that the measured

surface energy density is time dependent. Values ranging from 1.7 in\#/in^2 for $t_f \approx 1$ minute to 0.06 in\#/in^2 for $t_f \approx 20$ minutes were obtained. Similar observations have been made in cohesive fracture and the investigators defined the time rate of change of surface energy as (48)

$$\dot{S} = \gamma(t) \frac{dA}{dt} \quad (3.30)$$

Then inclusion into the thermodynamic power equation for fracture criticality is straightforward.

While such energy balances have not been made for the visco-elastic adhesion problem (due to computational difficulties), one would expect them to be quite similar to the cohesive fracture relations.

The use of oil as a pressurizing medium also influenced the calculated adhesive fracture energy. As a matter of fact, this value was reduced below the measuring capability of the test apparatus. It is interesting to note that other investigators have used the fracture energy interpretation for studying environmental effects such as ozone attack in rubber. (49)

3.3 PROBLEMATIC APPROACH

With the advent of the continuum interpretation of adhesion and development of some simple, easily applied tests, the scope of adhesion problems that may be quantitatively attacked suddenly broadens. That is not to say that analytical solutions can be immediately obtained for every problem for every material, nor that the nature of

adhesive surface energy is well understood; but at the very least, an engineering approach is now available to quantitize adhesive fracture for comparisons between geometry and loading conditions. There is a philosophical point, however, concerning the oscillating stress singularities for a crack at the bimaterial interface. Because of the trig-log behavior, one cannot rigorously compute the strain energy directly. Malyshev and Salganik⁽³³⁾ circumvent the difficulty by noting the improbability that the crack surfaces penetrate each other as indicated by the mathematical relations. Perlman and Sih⁽⁵⁰⁾ point out also that any technical material at the crack tip will have exceeded its elastic limit. As a practical matter, they disregard the oscillating singularity as does England.⁽⁵¹⁾

To demonstrate the approach a design engineering might take, consider two problems:

- a) An elastic solid propellant grain tending to debond from its case through pressurization or acceleration loads, and
- b) A reinforcing fiber tending to debond from its matrix material through tension on the fiber. These are basically similar problems and results are directly comparable.

3.3.1 *Solid Rocket Problem*

Recall that for linearly elastic systems where kinetic contributions may be considered negligible, the energy balance relation that describes adhesive fracture criticality is:

$$\frac{\partial U}{\partial A} = \gamma_a \quad (3.31)$$

where γ_a = adhesive surface energy density
 U = strain energy
 A = fracture area.

It is recognized, therefore, that in order to define criticality conditions for an arbitrary body, it is

- a) necessary to find the strain energy due to the loading, and
- b) describe the manner this strain energy changes with fracture surface area.

The strain energy⁽⁵²⁾ may be described as

$$U = \int_{vol} W \, d \, vol \quad (3.32)$$

where

$$W = \left(\frac{\lambda}{2} + \mu\right)e^2 - 2\mu e_2 - (3\lambda + 2\mu)e\alpha\Delta T + \frac{3}{2}(3\lambda + 2\mu)(\alpha\Delta T)^2 \quad (3.33 \, a)$$

or

$$\begin{aligned} W = & \frac{\lambda}{2} (\epsilon_x + \epsilon_y + \epsilon_z)^2 + \mu(\epsilon_x^2 + \epsilon_y^2 + \epsilon_z^2) + \frac{\mu}{2} (\gamma_{xy}^2 + \gamma_{xz}^2 + \gamma_{yz}^2) \\ & - (3\lambda + 2\mu) \alpha\Delta T (\epsilon_x + \epsilon_y + \epsilon_z) + \frac{3}{2} (3\lambda + 2\mu) (\alpha\Delta T)^2 \end{aligned} \quad (3.33 \, b)$$

where

- W = strain energy density
- λ, μ = Lamé's constants
- e = first strain invariant
- e_2 = second strain invariant
- α = coefficient of thermal expansion
- ΔT = temperature change

In order to find the strain distribution throughout the arbitrary loaded body in question and to subsequently integrate or sum the strain energy densities over the volume, it is frequently necessary to use a finite element stress analysis computer program. Such a program calls for

- a) Idealization of the body as an assembly of simple (usually triangular) elements attached at nodal points.
- b) Determining the stiffness coefficients for each individual element.
- c) Displaying the coefficients in a two-dimensional array or matrix. These, when summed, represent the stiffness coefficients for the idealized structure.
- d) Specifying applied loads and boundary restraints.

The unknown displacements at each nodal point are found through inversion of the matrix of stiffness coefficients relating these displacements to the specified loads. Strains, stresses, and reaction forces are then calculated from the displacements.

The inclusion of a routine for calculating the strain energy

for each individual element is a relatively simple task, and then, of course, the total strain energy is just the sum over all the elements.

In this effort the program described in reference (53) was used to find elastic strain energies developed in axisymmetric bodies subjected to pressure and acceleration loads. A number of computer runs were made differing only in that the fracture length was changed incrementally in the area of interest.

Shown in Figure 22 is a sketch of the idealization of the body into an assembly of elements. Since we are interested in debonding around the periphery of the grain end, the elements were made smaller and more dense in that region. Those familiar with finite element techniques recognize that the size and shape of the elements affect the rapidity of the matrix solution and the accuracy of the results. This is particularly true for bodies containing sharp geometric discontinuities such as this one does. The art that has developed for treatment of this particular difficulty involves making reasonably small elements near the apex of the crack, defining a region of these elements in the neighborhood of the apex, and then moving the entire package progressively deeper into the body to simulate fracture. This has been approximated by making series of identical elements along the crack trajectory. There are errors introduced by such modeling, but these are certainly overshadowed by other assumptions such as considering the solid propellant to be linearly elastic.

Continuing with the geometry description, the outer boundaries were held fixed, which would correspond to a rigid rocket motor case.

One end of the grain was held fixed in the pressure calculations, but was considered free in the longitudinal acceleration calculations. The boundary near the center line was fixed radially, but allowed to move longitudinally to simulate a solid or 100% web fraction grain.

The results of the energy calculations for a 9 inch radius grain, 17 inches long, having a modulus of 10^4 psi, Poisson's ratio of 0.485 and loaded by a pressure of 1000 psi are shown in Figure 23. Three modes of end release were investigated. One, designated as curve B, is probably the most physically realistic situation in a burning solid propellant grain. These data were obtained by successive computer runs in which the crack lengths were increased. The inverse square root of the slope of these curves was then taken to produce the curves shown in Figure 24. These normalized data form the parametric curves, somewhat akin to shape factor curves, for use in design. These, when using the appropriate parameters, are the debonding failure criteria for pressure loadings on an axisymmetric body, bonded to a rigid container. It is noted that the adhesive surface energy density, γ_a , is one of the parameters necessary for evaluation of the curves. This adhesive surface property may be obtained as described in references (31, 45). It should be noted that the left hand portion of the curve, for a $s/b < 0.04$ was constructed from theoretical relationships while the remainder of the curve was derived from the computer output. It may also be noted that the asymptotic value on the right hand extremes of the curves do not agree with what is expected from an infinite grain theoretical solution.⁽⁵⁴⁾ It is thought this discrepancy is due to the relatively short grain length

used in the idealized model. The L/D of the model is only 1.89 or $L/R = 3.78$. It is noted that similar discrepancies were obtained in reference (53); Figure 16 for $L/R = 4.0$.

An acceleration loading of 100g's was placed on the same idealized geometry except that the ends of the axisymmetric body were considered to be free. Again, the strain energy was calculated for various release areas (see Figure 25). The slope and the inverse of the square root of the slope were obtained with the latter being shown in Figure 26.

The idealized model used for acceleration has no transverse plane of symmetry, thus, the L/R ratio is 1.89. Hence, these results also are not comparable to the infinite length asymptote.

3.3.2 *Fiber Pull-out Problem*

In fiber reinforced composite materials, strong stiff fibers are imbedded in a matrix of lower density and modulus. If the materials are properly incorporated there results a light but strong material. Loads imposed on such materials are carried primarily through the fibers. Since it is very difficult to externally load all the fibers uniformly the matrix component serves to transfer loads through shear from highly loaded fibers to adjacent but low stressed fibers. The matrix must adhere to the fibers in order to implement this load transfer. This has been recognized for some time in the composites industry, particularly the rubber tire industry where evaluation tests for the bond strength are frequently run. The test currently used is a fiber

(steel) concentrically imbedded and cured in a cylinder of rubber, and then longitudinally pulled out. The force necessary to withdraw the fiber is designated the bond strength.

It is readily apparent that stresses will not be uniformly distributed along the fiber nor in the matrix material. Further investigation shows stress singularities to exist at the rubber surface where the fiber is inserted and at flaws in the bimaterial interface. This problem is basically similar to the solid rocket problem and will be treated in the same manner.

Mention will be again made concerning the nature of the stress singularity near the tip of a flaw. Philosophically speaking, known solutions are only applicable when the properties of the two materials are the same or when one material is incompressible and the other is rigid. Otherwise oscillations occur in the singularity and it is not integrable. It is emphasized that when the oscillations are ignored as a practical matter, errors of the order of the geometric region containing the oscillations, are introduced. Checks should always be made when the oscillating singularities exist.

Consider a stiff fiber tending to be withdrawn from an elastic but much lower modulus surrounding matrix. This may be modeled using the direct stiffness method. A half-section of the axisymmetric model is shown in Figure (27). For these computations, the mechanical properties of the fiber correspond to that of a carbon filament and those of the matrix correspond to an epoxy. Shown in Figure (28) are

the mechanical properties and boundary conditions used in the calculations.

Calculated strain energies versus released area for the particular load inputs are shown in Figure (29). The influence of unbond area on strain energy was also calculated for areas across the imbedded tip of the fiber (see Figure (30)). Comparison of these results (Figure (31)) indicate a propensity to debond at the matrix free surface for uniform adhesive surface energy density over the bond area.

IV. CONCLUSIONS

Cohesive and adhesive fractures have been studied both analytically and experimentally using their common link, continuum mechanics. The cohesive fracture studies were conducted assuming linear viscoelastic media and simplified geometry, whereas the adhesive fracture study assumed linear elastic media. Due to the difference in material assumptions and geometrics, the conclusions will be listed separately.

4.1 *COHESIVE-VISCOELASTIC FRACTURE*

1. Predictive fatigue relations were analytically derived for simple flaw geometries with displacement boundary conditions in a linearly viscoelastic material. These isothermal relations implicitly show the fatigue life to vary approximately with the inverse of the loss modulus.
2. Experimental fatigue test results were not as predicted due to temperature increases resulting from viscous energy dissipation in the test specimen.
3. Crack tip temperature measurements during dual frequency cyclic fatigue test graphically illustrate the importance of this parameter on fatigue life.
4. Thermomechanical coupling considerations are necessary for accurate development of fatigue fracture predictive relations. Qualitative arguments show the isothermal fatigue life predictions are low at imposed frequencies less than the frequency of maximum energy dissipation (ω_m), and high for frequencies greater than the frequency ω_m .

4.2 ADHESIVE-ELASTIC FRACTURE

1. A simple test for evaluating certain cases of adhesive fracture has been developed. Results are interpreted in terms of a fracture energy that may be used for comparative evaluation of materials and bonding processes and for engineering fracture analysis.
2. The flaw-size-load relationship developed by Williams⁽¹²⁾ assuming elastic fracture is experimentally verified.
3. Experimental indications are that adhesive fracture energy is time dependent, which suggests the need to include time dependent terms in the energy balance.
4. Until time dependent analyses become available, engineering applications of elastic fracture analysis are demonstrated by problem solutions.

Engineering applications of elastic fracture analysis are demonstrated by solutions to a solid rocket bonding problem and a fiber pull-out problem. These problems are by no means inclusive of the fracture problems that may be encountered. It is hoped the reader is encouraged to study fracture and contribute to the further development of this interesting field.

LIST OF REFERENCES

1. Galileo Galilei, "Discorsi e dimostrarayioni Matematiche intorno ad alcune Science attenanti alla meccanica ed i movimenti locali," translated by T. Salusbury, 2 Vols. Mathematical Collections and Translations, (London: Thames Press, 1661-1665).
2. W. Weibull, "A Statistical Theory of Strength of Materials," Ingeniors Vetenskaps Akademien - Handlingar, no. 151 (1939).
3. C. E. Inglis, "Stresses in a Plate Due to the Presence of Cracks and Sharp Corners," Trans. Inst. Naval Arch. 60 (1913), 219-230.
4. A. A. Griffith, "The Phenomena of Rupture and Flow in Solids," Philo. Trans. Roy. Soc. London, 221 (1921), 163-198.
5. D. C. Drucker, "A Continuum Approach to Fracture of Metals," Fracture of Solids, Vol. 20, (New York: Interscience Publishers, 1962).
6. V. Weiss and S. Yukawa, "Critical Appraisal of Fracture Mechanics," in Fracture Toughness Testing, ASTM Spec. Tech. Pub. 381, (Baltimore, Md.: American Society for Testing Materials, 1965).
7. A. H. Cottrell and D. Hull, "Extension and Intrusion by Cyclic Slip in Copper," Proc. Roy. Soc. London, A 242 (1957), 211-213.
8. E. Orowan, "Plasticity Aspects in Fracture," Inst. Engrs. Shipbuild. Scotland (1945), 165-171.
9. G. R. Irwin, "Fracture Dynamics," Fracturing of Metals, (Cleveland, Ohio: American Society for Metals, 1948).
10. I. N. Sneddon, "The Distribution of Stress in the Neighborhood of a Crack in an Elastic Solid," Proc. Roy. Soc. London, A-187 (1946), 229-260.
11. G. R. Irwin, "Analysis of Stresses and Strains Near the End of a Crack," J. Applied Mech., 24 (1957), 361-372.
12. M. L. Williams, "On the Stress Distribution at the Base of a Stationary Crack," J. Applied Mech., 24 (1957), 109-114.
13. J. A. H. Hult and F. A. McClintock, "Elastic-Plastic Stress and Strain Distribution Around Sharp Notches in Repeated Shear," IX Congr s International de M canique Appliqu e, 8 (1957), 51-58.

14. E. Folias, "On the Theory of Fracture of Curved Sheets," University of Utah College of Engr. Report No. UTEC CE 68-096 (1968)
15. D. S. Dugdale, "Yielding of Steel Sheets Containing Slits," J. Mech. Phys. Solids, 8 (1960), 100-104.
16. L. J. Broutman and F. J. McGarry, "Fracture Surface Work Measurements on Glassy Polymers by a Cleavage Technique," J. Appl. Poly. Sci., 9 (1965), 589-608
17. R. S. Rivlin and A. G. Thomas, "Rupture of Rubber, Part I," J. Poly. Sci., 10 (1953), 291-299.
18. J. P. Berry, "Dependence of the Fracture Surface Energy on Temperature and Molecular Structure," J. Poly. Sci., A 1 (1963), 993-998.
19. M. L. Williams, "Initiation and Growth of Viscoelastic Fracture," Int. J. Frac. Mech., 1, (1965), 292-310.
20. M. L. Williams, F. R. Wagner and W. Knauss, "Fatigue Failure in Linearly Viscoelastic Materials," Bull. 5th Mech. Behavior Work. Grp. Mtg., Interagency Chemical Rocket Propulsion Group, (October 1966), 681-692.
21. W. B. Jones, F. R. Wagner and M. L. Williams, "Cumulative Damage in the Mechanics of Viscoelastic Fracture," Bull. 6th Mech. Behavior Work. Grp. Mtg., Interagency Chemical Rocket Propulsion Group (October 1967), 393-405.
22. J. S. Noel, J. D. Burton and B. C. Harbert, "Fracture Mechanics Approach to Cumulative Damage," Air Force Rocket Propulsion Lab. Tech. Rep. No. 68-132 (December 1968).
23. R. J. Farris and J. E. Fitzgerald, "Deficiencies of Viscoelastic Theories as Applied to Solid Propellants," Bull. 1st Joint Army, Navy, NASA, Air Force Mtg. (November 1969).
24. F. A. McClintock and A. S. Argon, Mechanical Behavior of Materials, (Reading, Massachusetts: Addison Wesley, 1966).
25. D. J. Alner, Aspects of Adhesion, (London: University of London Press, 1966).
26. W. H. Keesom, "Originalmitteilungen," Phys. Zeit., 22, (1921), 129-141.
27. P. Debeye, "Molekularkrafte and ihre elektrische Deutung," Phys. Zeit., 22, (1921), 302-308.
28. F. London, "The General Theory of Molecular Forces," Trans. Faraday Soc., 33, (1937), 8-26.

29. R. L. Patrick, Treatise on Adhesion and Adhesives, (New York: Marcel Dekker, Inc., 1967).
30. R. Houwink and G. Salomon, Adhesives and Adhesion, Vol. 1, (Amsterdam: Elsevier Publishing Company, 1967).
31. M. L. Williams, "The Continuum Interpretation for Fracture and Adhesion," J. Appl. Poly Sci., 13 (1969), 29-40.
32. M. L. Williams, "The Stresses Around a Fault or Crack in Dissimilar Media," Bull. Seis. Soc. Amer., 49, (1959) 199-204.
33. B. M. Malyshev and R. L. Salganik, "The Strength of Adhesive Joints Using the Theory of Cracks," Int. J. Frac. Mech., 1, (1965), 114-128.
34. H. Dannenberg, "Measurement of Adhesion by a Blister Method," J. Appl. Poly. Sci., 5, (1961), 125-134.
35. P. C. Paris and G. C. Sih, "Stress Analysis of Cracks," Fracture Toughness Testing, ASTM Spec. Tech. Pub. 381, (Baltimore, Md.: American Society for Testing Materials, 1965).
36. G. Lindsey, "Hydrostatic Tensile Fracture of a Polyurethane Elastomer," unpublished Ph.D. Dissertation, California Institute of Technology, Pasadena, California, 1965.
37. M. L. Williams, "The Kinetic Energy Contribution to Fracture Propagation in a Linearly Viscoelastic Material," Int. J. Fract. Mech., 4 (1968), 69-78.
38. J. D. Burton and J. S. Noel, "Viscoelastic Fracture in Plane Stress and Plane Strain Fields," Bull. 6th Mech. Behavior Work. Grp. Mtg., Interagency Chemical Rocket Propulsion Group (October 1967), 357-375.
39. J. F. Tavernelli and L. F. Coffin, "A Compilation and Interpretation of Cyclic Strain Fatigue Tests on Metals," Am. Soc. Metals, 51 (1959), 438-453.
40. M. G. Beeley, "Fatigue in Viscoelastic Materials with an Initial Flaw," unpublished Master's Thesis, Department of Mechanical Engineering, University of Utah, 1968, also University of Utah College of Engineering Report No. UTEC D0 68-060 (1968).
41. O. L. Bowie, "Analysis of an Infinite Plate Containing Radial Cracks Originating at the Boundary of an Internal Circular Hole," J. Math. and Phys., 35 (1956), 60-71.

42. V. Arpaci, Conduction Heat Transfer, (Reading, Massachusetts: Addison Wesley, 1966).
43. M. L. Williams et al., "The Mechanical and Optical Characterization of Solithane 113 and Investigation of Optical Lag in Photo-viscoelastic Analysis," California Institute of Technology, GALCIT WL-TR-64-155 (1964).
44. S. Timoshenko and S. Woinowsky-Krieger, Theory of Plates and Shells, (New York: McGraw-Hill Book Company, 1959).
45. W. B. Jones, "A Simple Test for Certain Cases of Adhesion," University of Utah, College of Engr. Report No. UTEC DO 69-088 (1969),
46. H. M. Berger, "A New Approach to the Analysis of Large Deflection of Plates," J. Appl. Mech., 22 (1955), 465-471.
47. F. H. Selto, "Adhesive Fracture Using Large Plate Deflections," unpublished Master's Thesis, Department of Mechanical Engineering, University of Utah, 1969, also College of Engineering Report No. UTEC DO 69-067 (1969).
48. S. J. Bennett, G. P. Anderson, and M. L. Williams, "The Time Dependence of Surface Energy on Cohesive Fracture," University of Utah, College of Engr. Report No. UTEC DO 69-072 (1969). (also accepted for publication in J. Appl. Poly. Sci.).
49. G. Salomon and F. Van Bloois, "Correlations Between Structure of Elastomers and the Mechanism of their Degradation by Ozone," J. Appl. Poly. Sci., 7 (1963), 1117-1132.
50. A. B. Perlman and G. C. Sih, "Elastostatic Problems of Curvilinear Cracks in Bonded Dissimilar Materials," Int. J. Engr. Sci., 5 (1967), 845-867.
51. A. H. England, "A Crack Between Dissimilar Media," J. Appl. Mech., 32 (1965), 400-402.
52. I. S. Sokolnikoff, Mathematical Theory of Elasticity, 2nd Ed., (New York: McGraw-Hill Book Company, 1956).
53. J. S. Noel and L. D. Webb, "The Role of Fracture Mechanics in the Design of Optimum Grain-Case Terminations," Bull. 5th Mech. Behavior Work. Grp. Mtg., Interagency Chemical Rocket Propulsion Group (October 1966), 351-364.
54. M. L. Williams and T. Kunio, "An Analysis of Adhesive Debonding in Case-Bonded Solid Rocket Motors," Presentation at the International Symposium on Science and Technology of Space, Tokyo, Japan, August 1969.

APPENDIX A.

TABLE 1
Stress Intensity Factor, K_1 , for Various Geometries

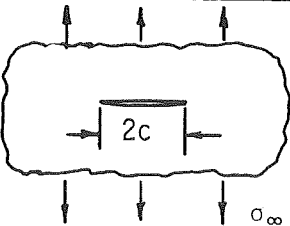
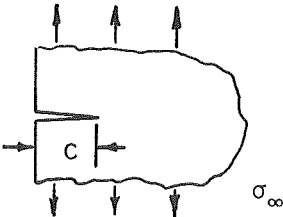
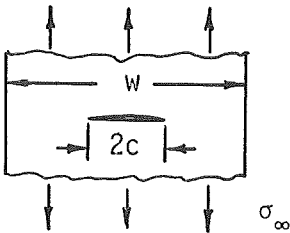
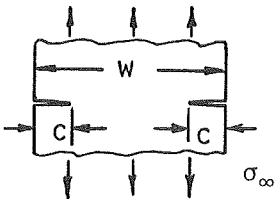
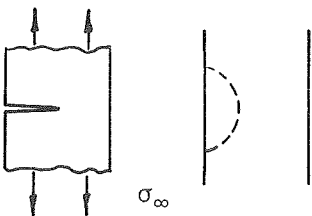
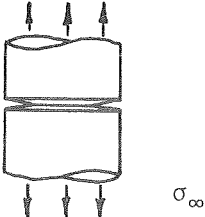
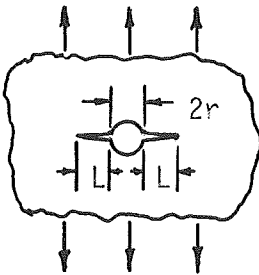
Configuration	K_1
	$\sigma_{\infty} C^{\frac{1}{2}} \pi^{\frac{1}{2}}$
	$1.1 \sigma_{\infty} C^{\frac{1}{2}} \pi^{\frac{1}{2}}$
	$\approx \sigma_{\infty} C^{\frac{1}{2}} \left(\frac{W}{C} \tan \frac{\pi C}{W} \right)^{\frac{1}{2}}$
	$\approx \sigma C^{\frac{1}{2}} \sqrt{\frac{W}{\pi C} \tan \frac{\pi C}{W}} \quad \times$ $\sqrt{1 + 0.2 \cos \frac{\pi C}{W}}$
	$\approx 1.1 \sigma C^{\frac{1}{2}} \pi^{\frac{1}{2}}$
	$K_1 = \sigma_{\text{net}} \pi D^{\frac{1}{2}} F(d/D)$

TABLE 1 (cont.)

d/D	F(d/D)	d/D	F(d/D)
0	0	.6	.238
.1	.111	.7	.240
.2	.155	.8	.233
.3	.185	.9	.205
.4	.209	1.0	0.
.5	.227		


$$K_I = \sigma_\infty \sqrt{\pi L} F(L/r)$$

L/r	F(L/r)	L/r	F(L/r)
0	3.39	.6	1.71
.1	2.73	.8	1.58
.2	2.41	1.0	1.45
.3	2.15	10.	1.03
.4	1.96	∞	1.00
.5	1.83		

RAW TEST DATA

Table 2

CONSTANT FREQUENCY TESTS

Test No.	Frequency c/m	Cycles to Failure	Crack Growth
100	515	868	.001"
101	1000	984	.0014"
102	3000	1030	
103	3000	1048	
104	4000	1340	
105	4000	1337	

Table 3

MULTIPLE FREQUENCY TESTS

Test No.	F ₁ c/m Initial Frequency	F ₂ c/m Final Frequency	Cycles @ F ₁	Cycles @ F ₂	Crack Growth
601	1000	5000	323	677	.0016"
602	1000	5000	323	727	
603	5000	1000	700	255	.001"
604	5000	1000	700	236	
606	650	5000	500	700	.0022"
607	650	5000	500	800	.0022"
608	650	5000	500	660	.0016"
609	5000	650	700	480	.0014"
610	5000	650	700	430	.0014"
611	5000	650	700	370	.0020"
613	515	4000	500	700	
614	515	4000	500	800	.0016"
615	515	4000	500	700	
617	4000	515	725	275	.0014"
618	4000	515	725	295	.0012"

Table 4

AVERAGE CYCLES TO FAILURE

Initial Frequency c/m	Final Frequency c/m	Total Cycles at Failure	% Difference
1000	5000	1025	+ 7.8%
5000	1000	945	
650	5000	1220	+ 7.7%
5000	650	1126	
515	4000	1233	+ 18.1%
4000	515	1010	

APPENDIX B.

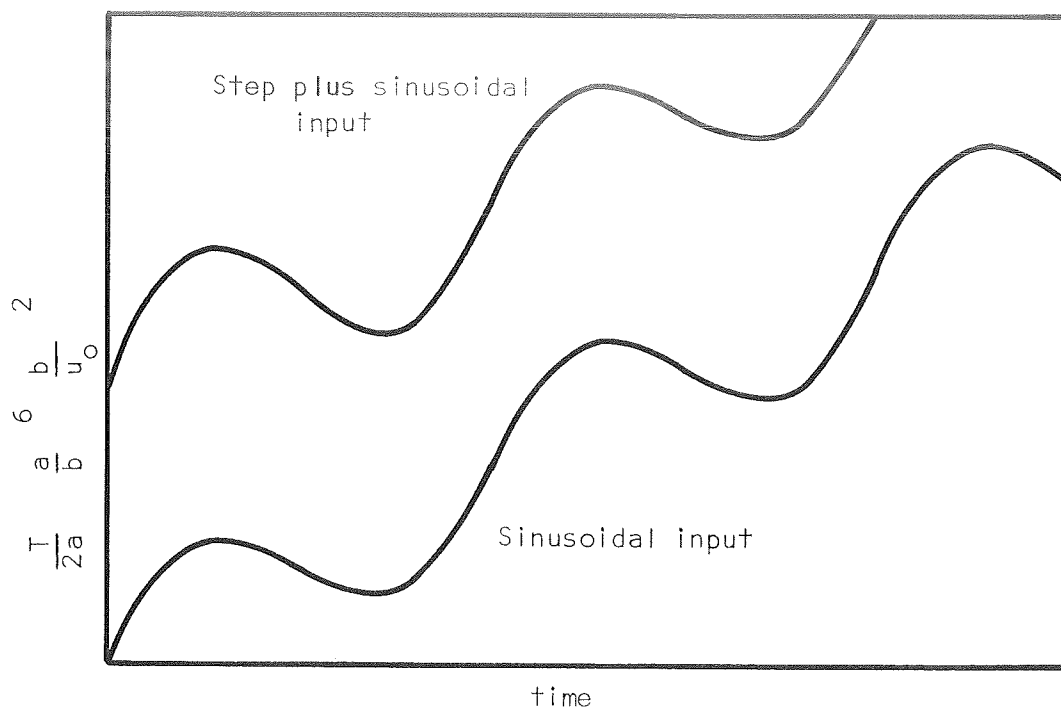


Figure 1. Comparison of the propagating flaw solutions for two loading conditions

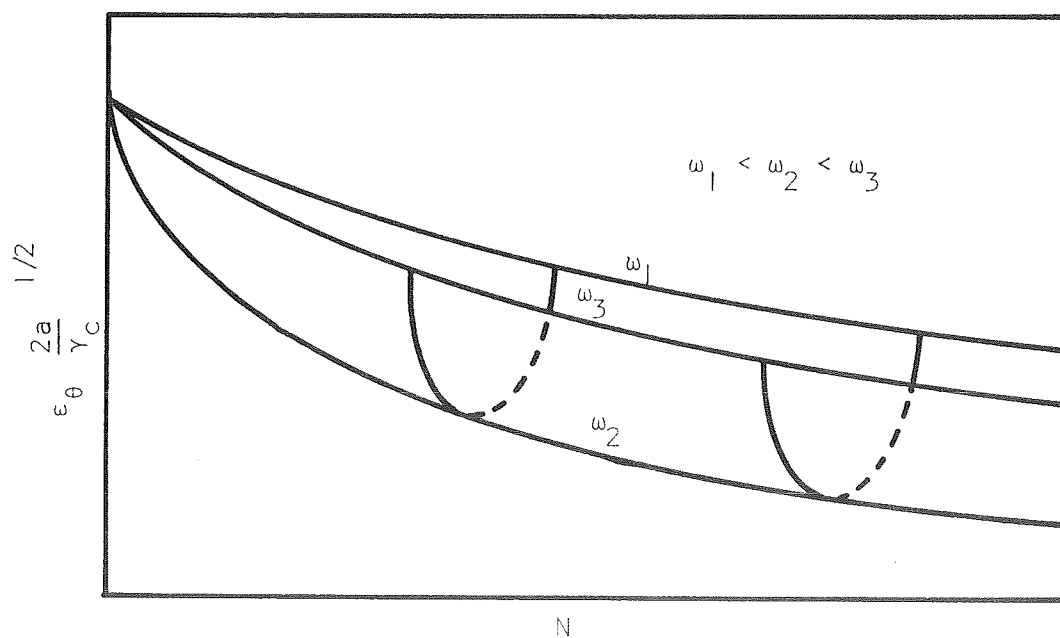


Figure 2. Dependence of fatigue life on frequency for viscoelastic material

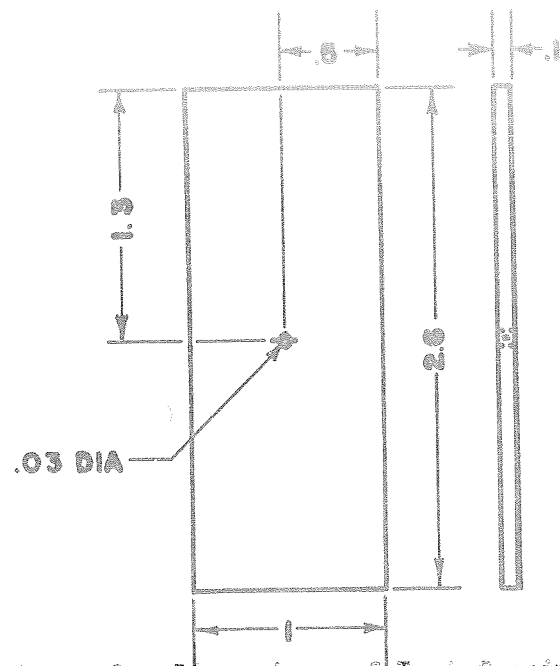


Figure 3. Dimensions of Test Specimen

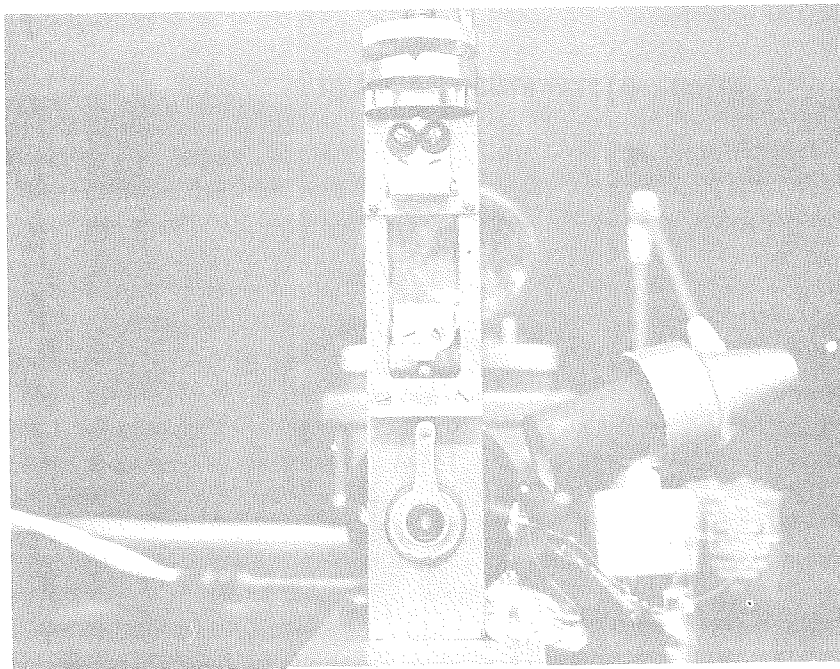


Figure 4. Test Machine

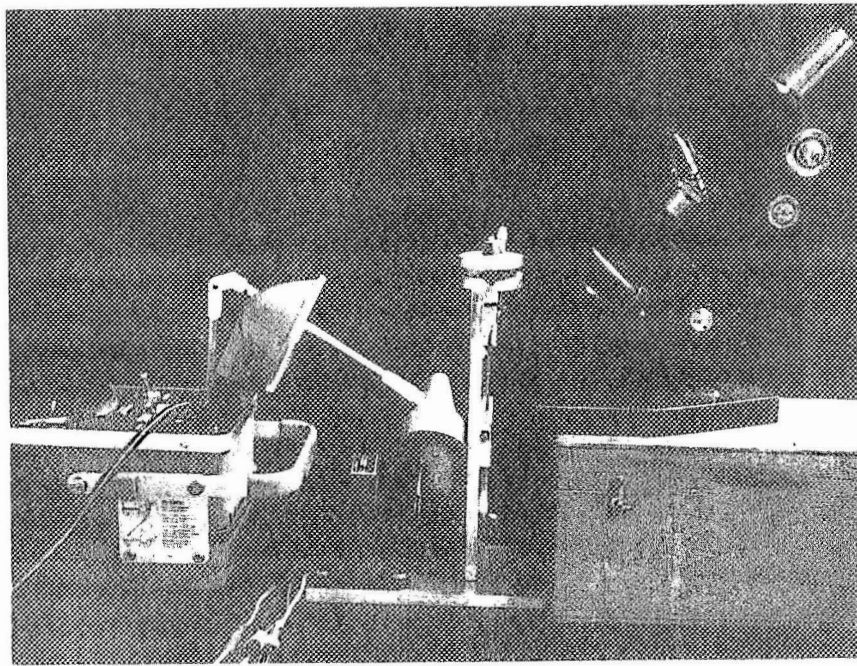


Figure 5. Observation Angle

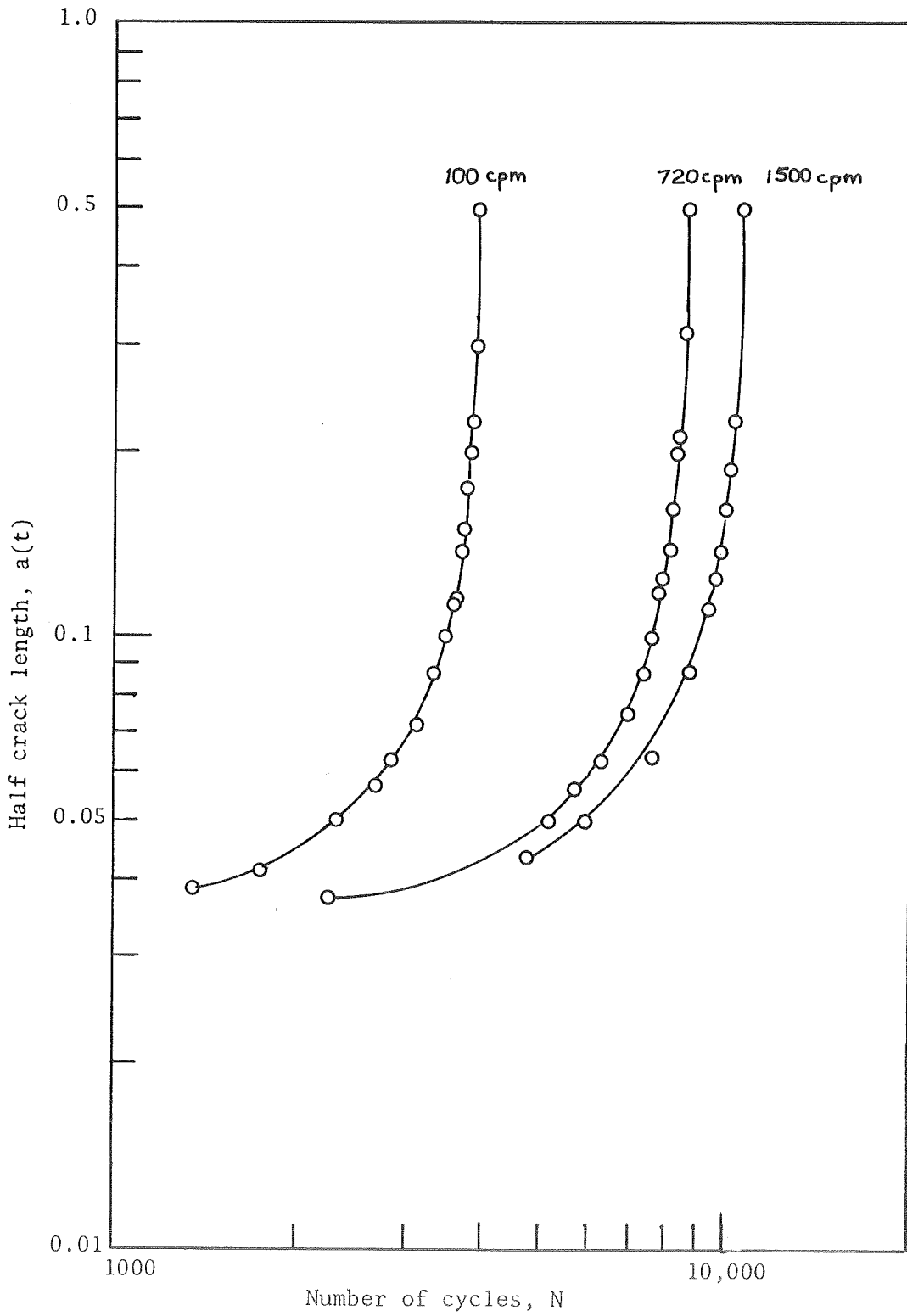


Figure 6. Crack length versus number of cycles for simple tension fatigue tests on Solithane 113

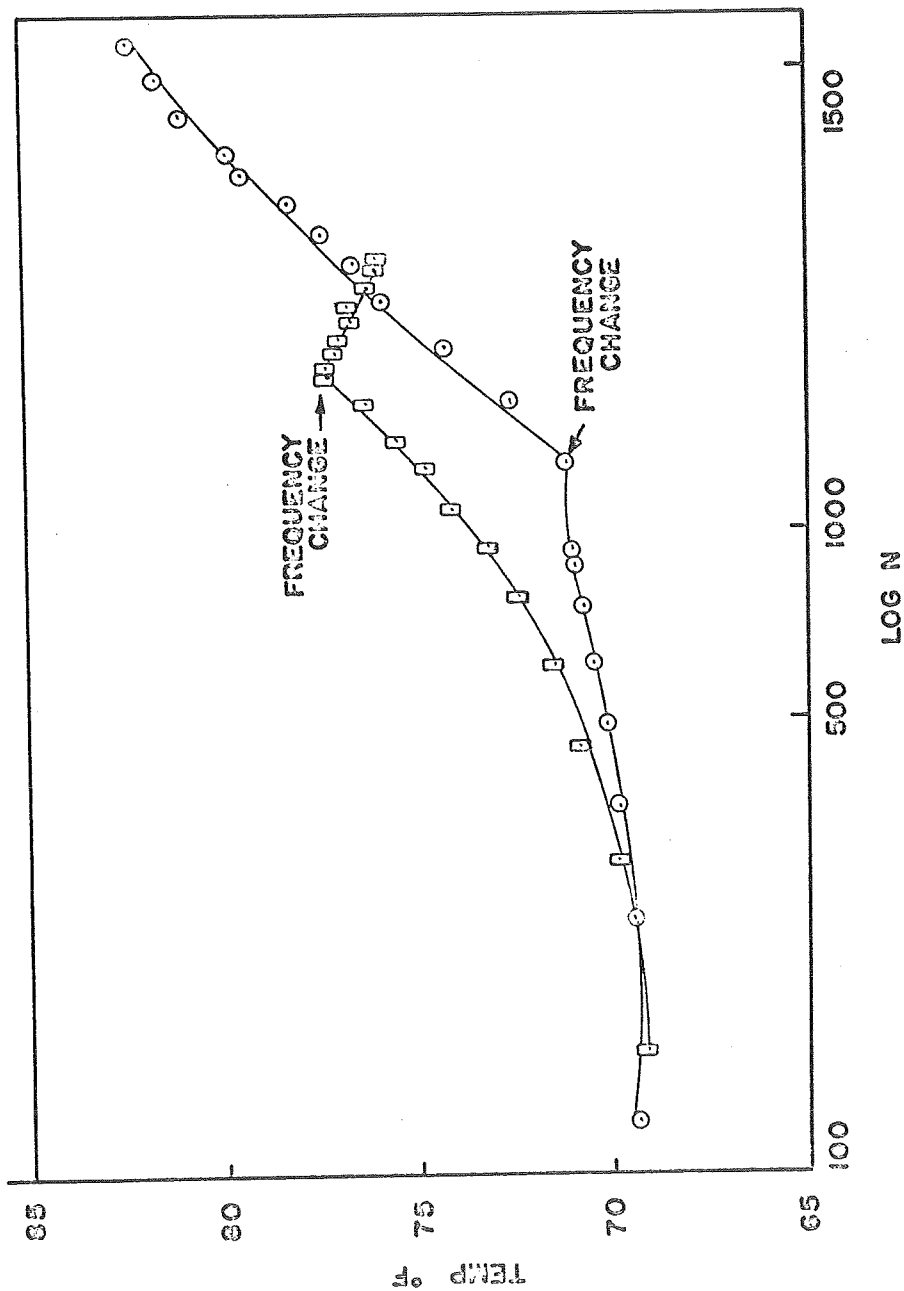


Figure 7 Temperature near Crack Tip vs Fatigue Cycles with Multiple Frequencies and Sequence Reversal upper curve at 4000 c/m then 800 c/m; lower curve at 800 c/m then 4200 c/m.

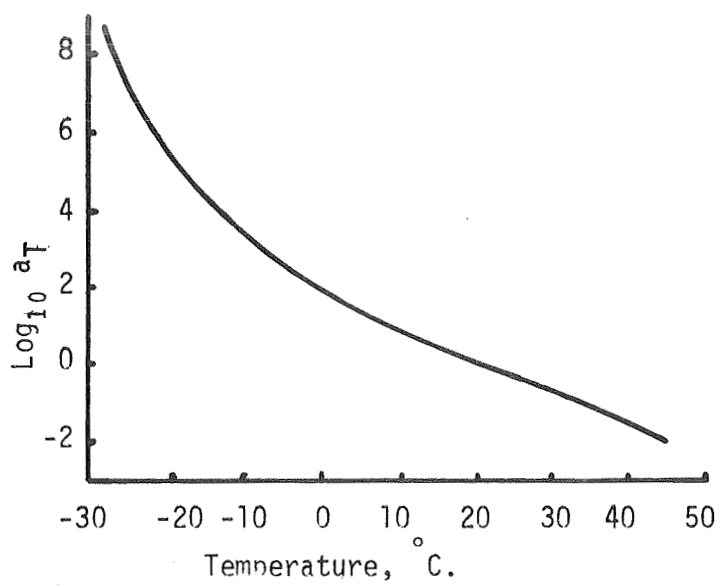


Figure 8 WLF Curve for GALCITI (43)

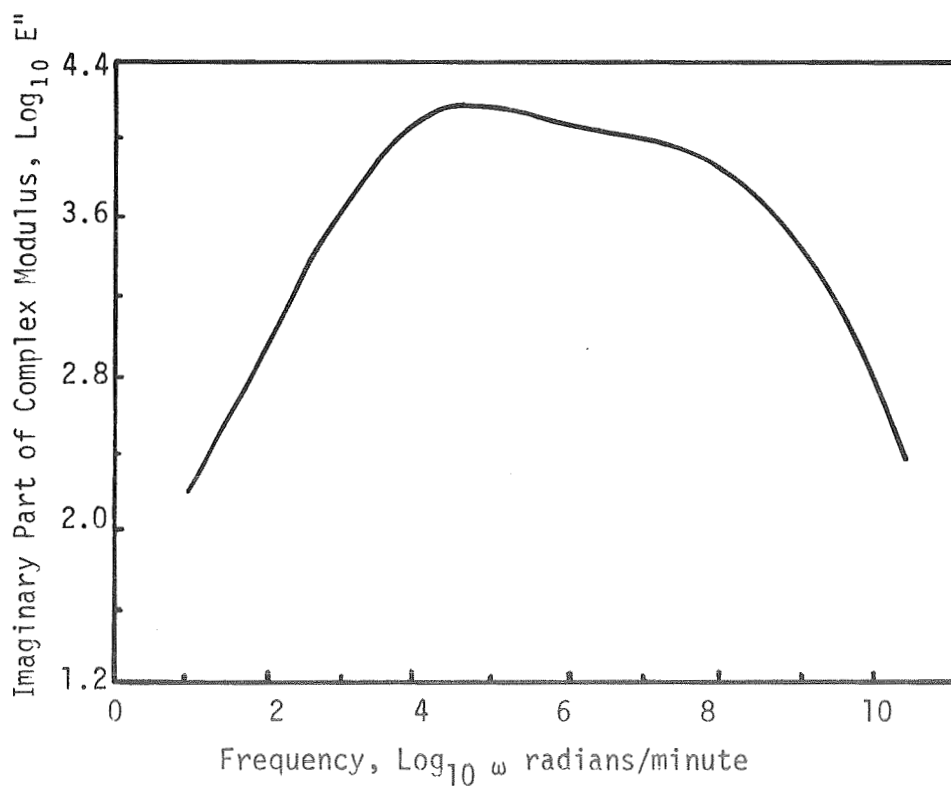


Figure 9 $E''(\omega)$ (loss modulus) vs. Frequency Curve for GALCITI (43)

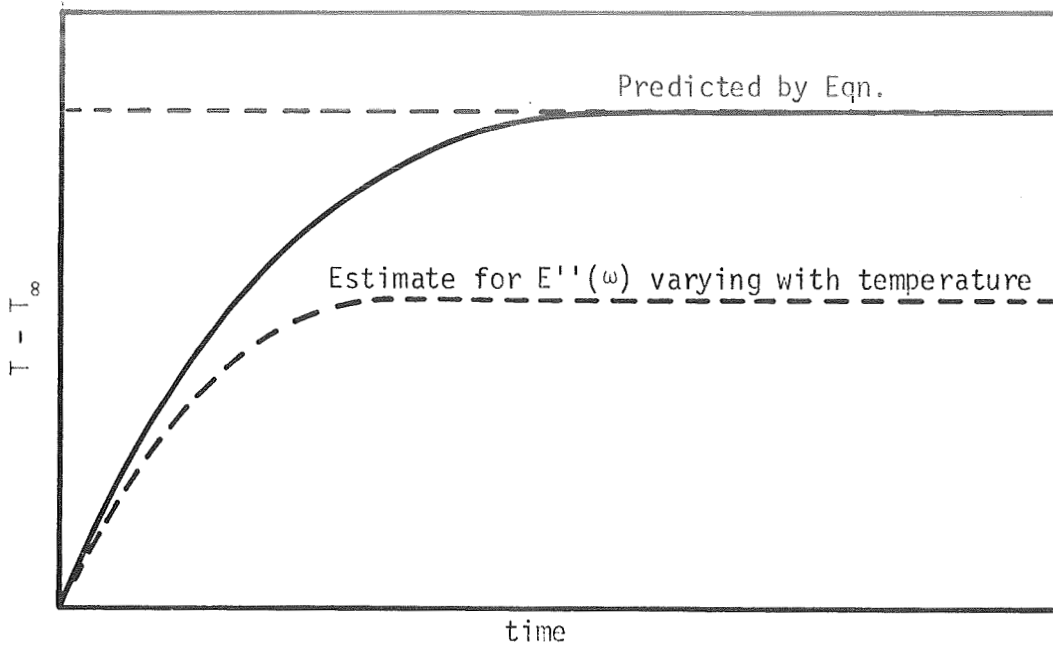


Figure 10. Estimated temperature rise vs. time for a viscoelastic sample in uniaxial cyclic fatigue ($\omega < \omega_m$)

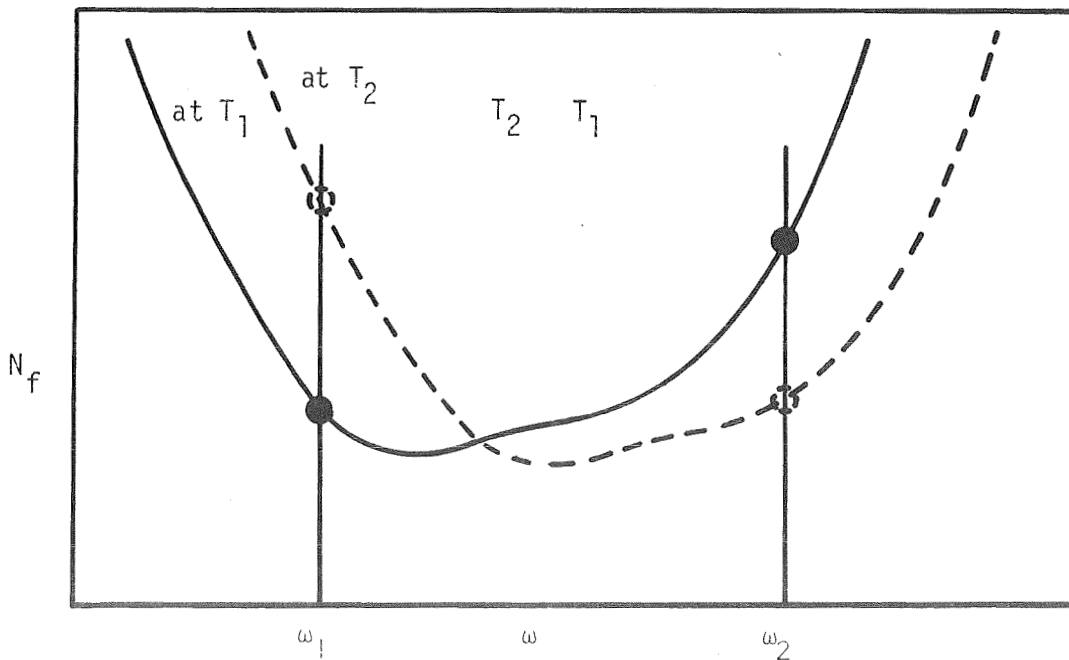


Figure 11. Estimated change of fatigue life at constant frequency due to temperature increase

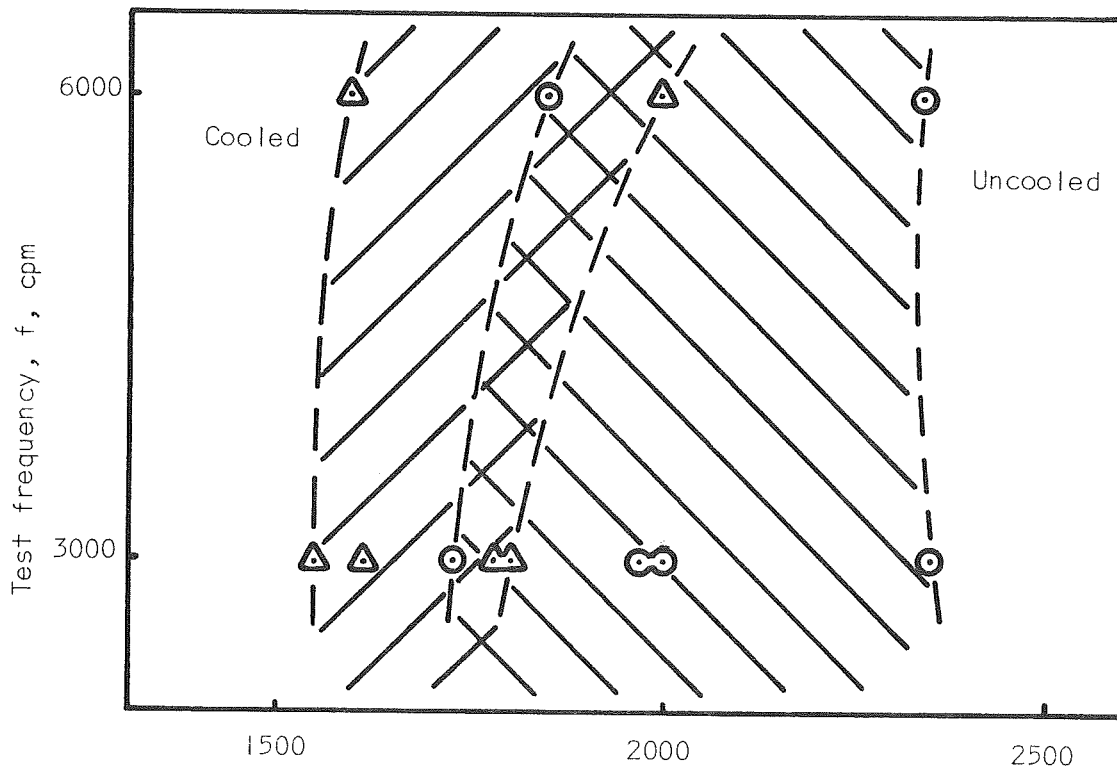


Figure 12. Comparison of fatigue life for fan cooled and uncooled samples

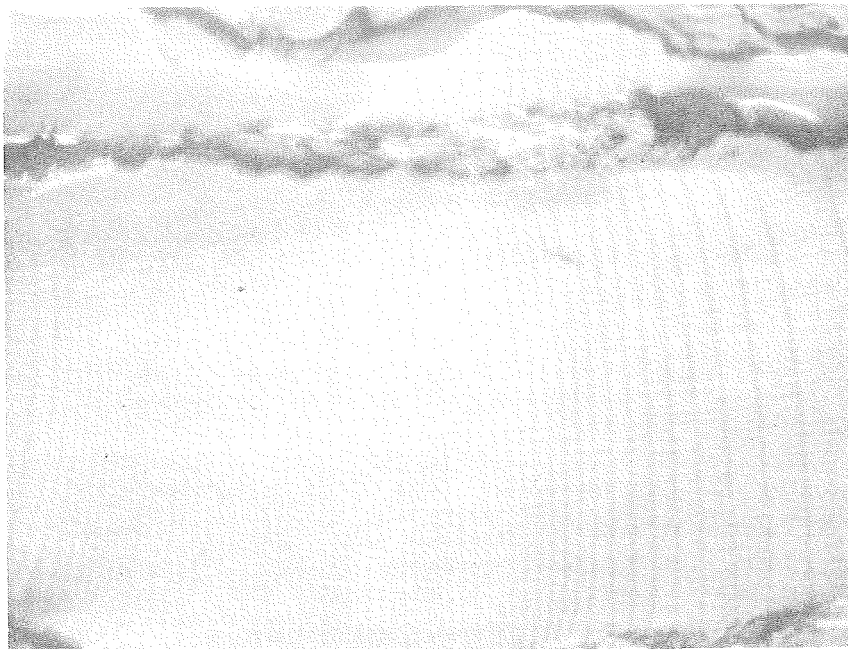


Figure 13. Optical microphotograph of GALCIT I fatigue fracture surface (100x)

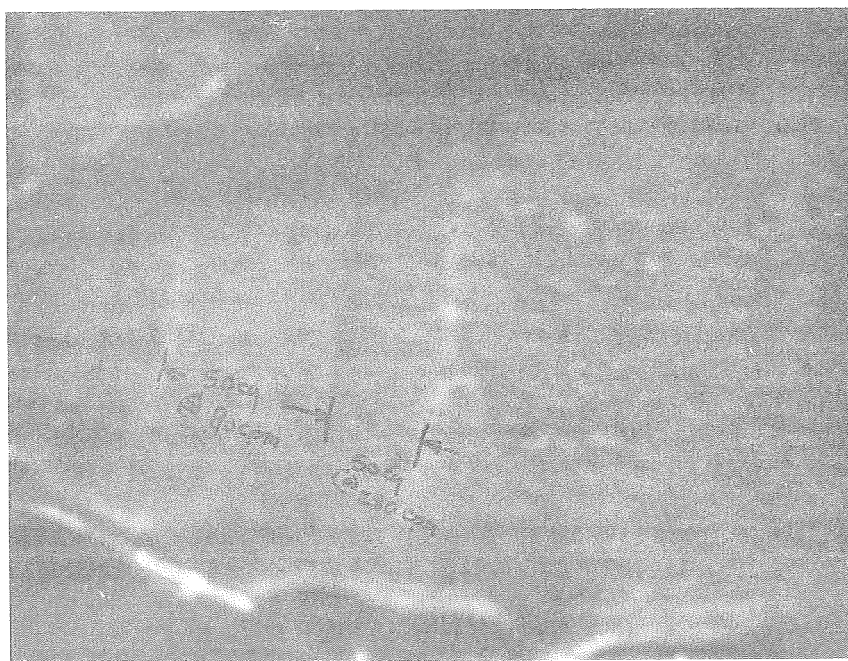


Figure 14. Optical microphotograph showing surface effects of dual frequency fatigue (100x)

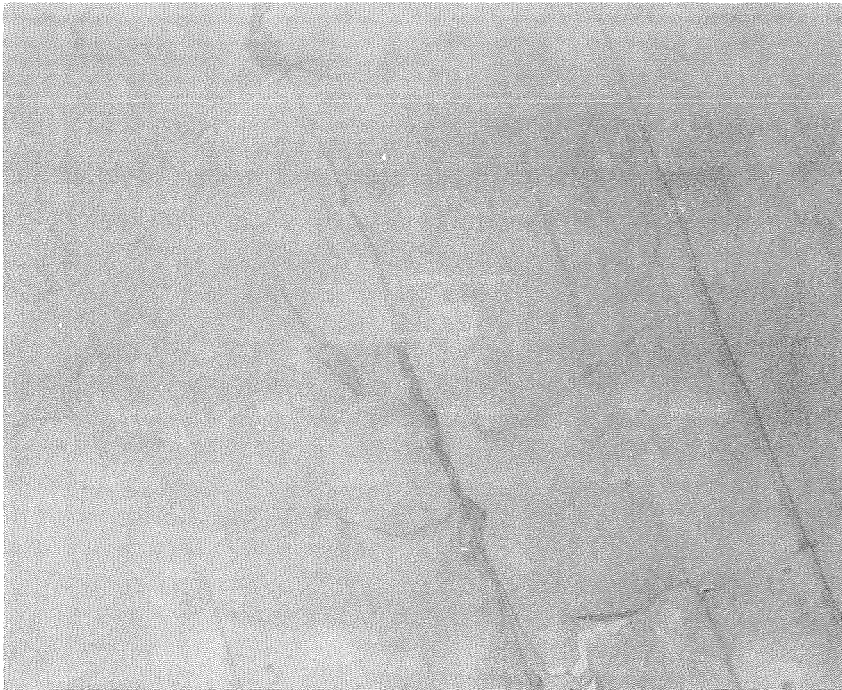


Figure 15. Transmission electron microscopic photograph showing fatigue striations (13,500x)



Figure 16. River markings resulting from a tear test (70x)

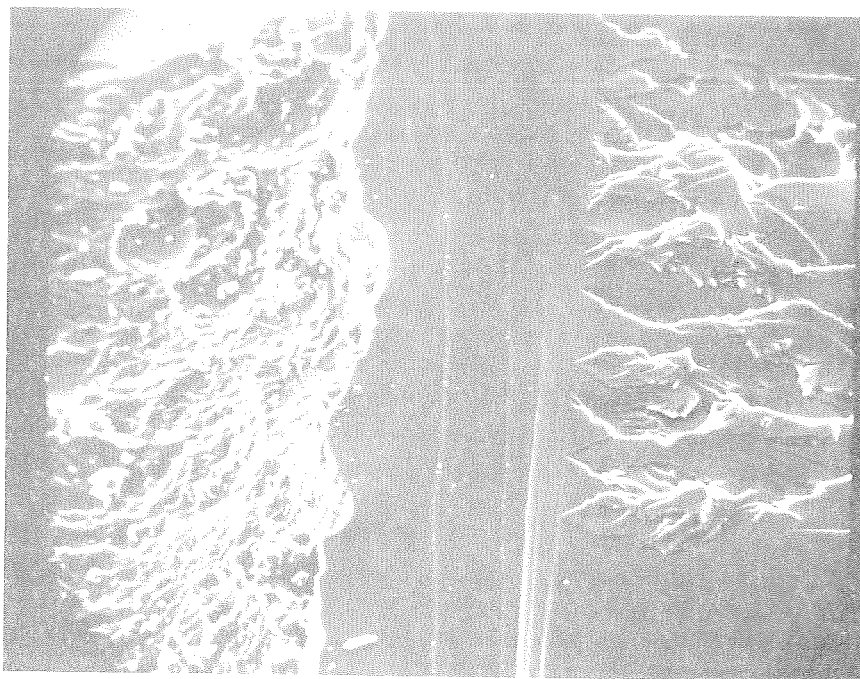


Figure 17. Tear fracture surface from an incomplete fatigue test (120x)

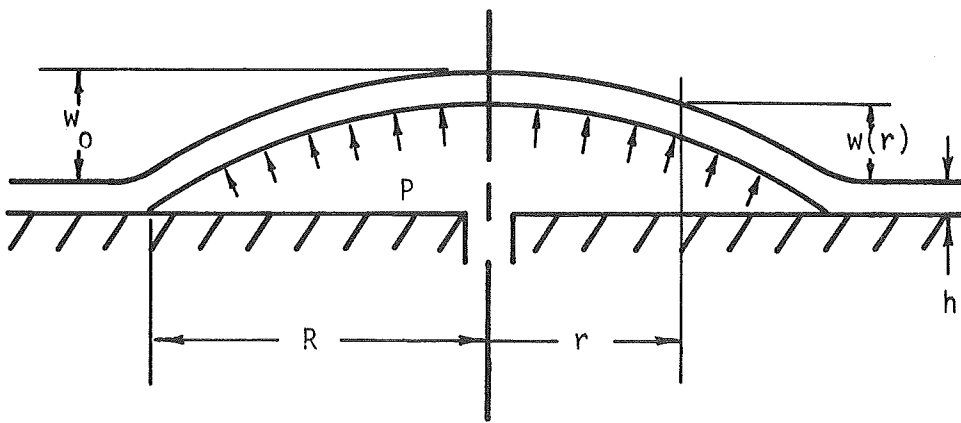


Figure 18 Sketch of the deflected plate

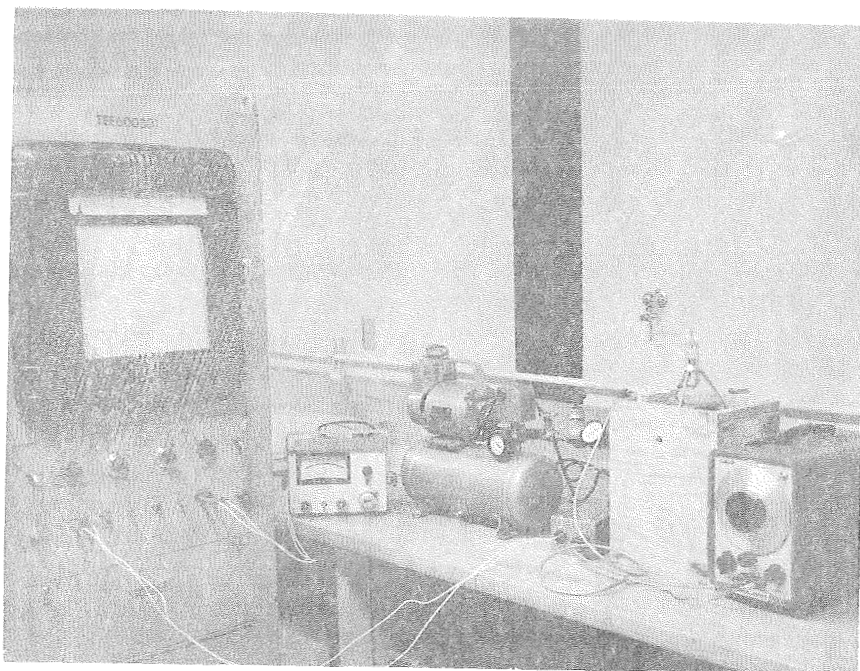


Figure 19-a. Photograph of blister test apparatus

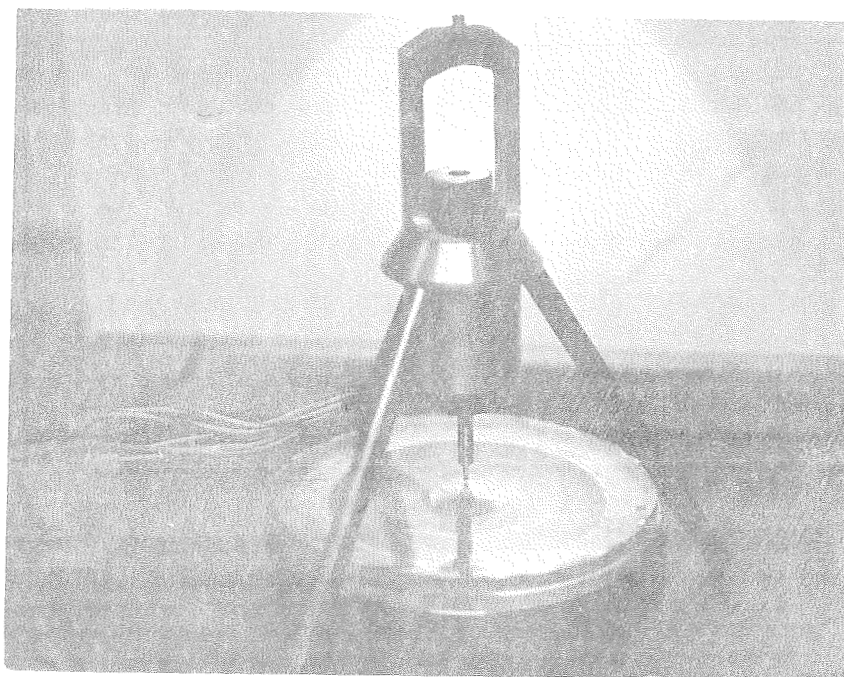


Figure 19-b. A blister test in progress

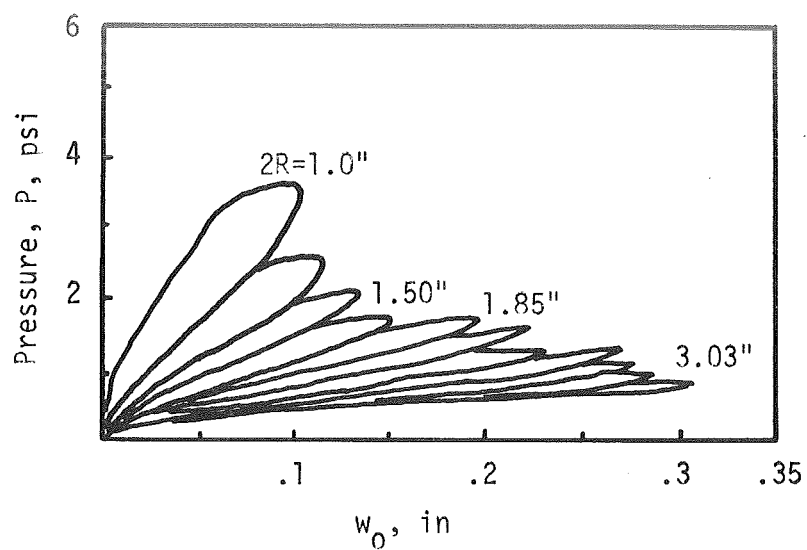


Figure 20 Typical pressure versus deflection test data

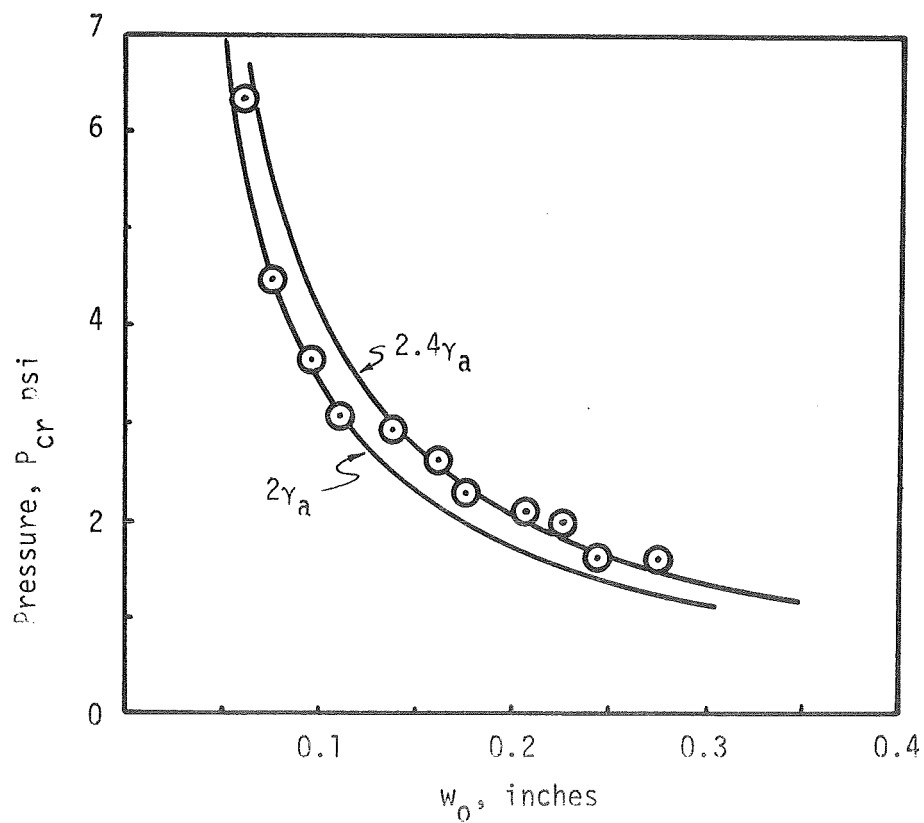


Figure 21 Plot of the critical pressure versus center deflection from a blister test.

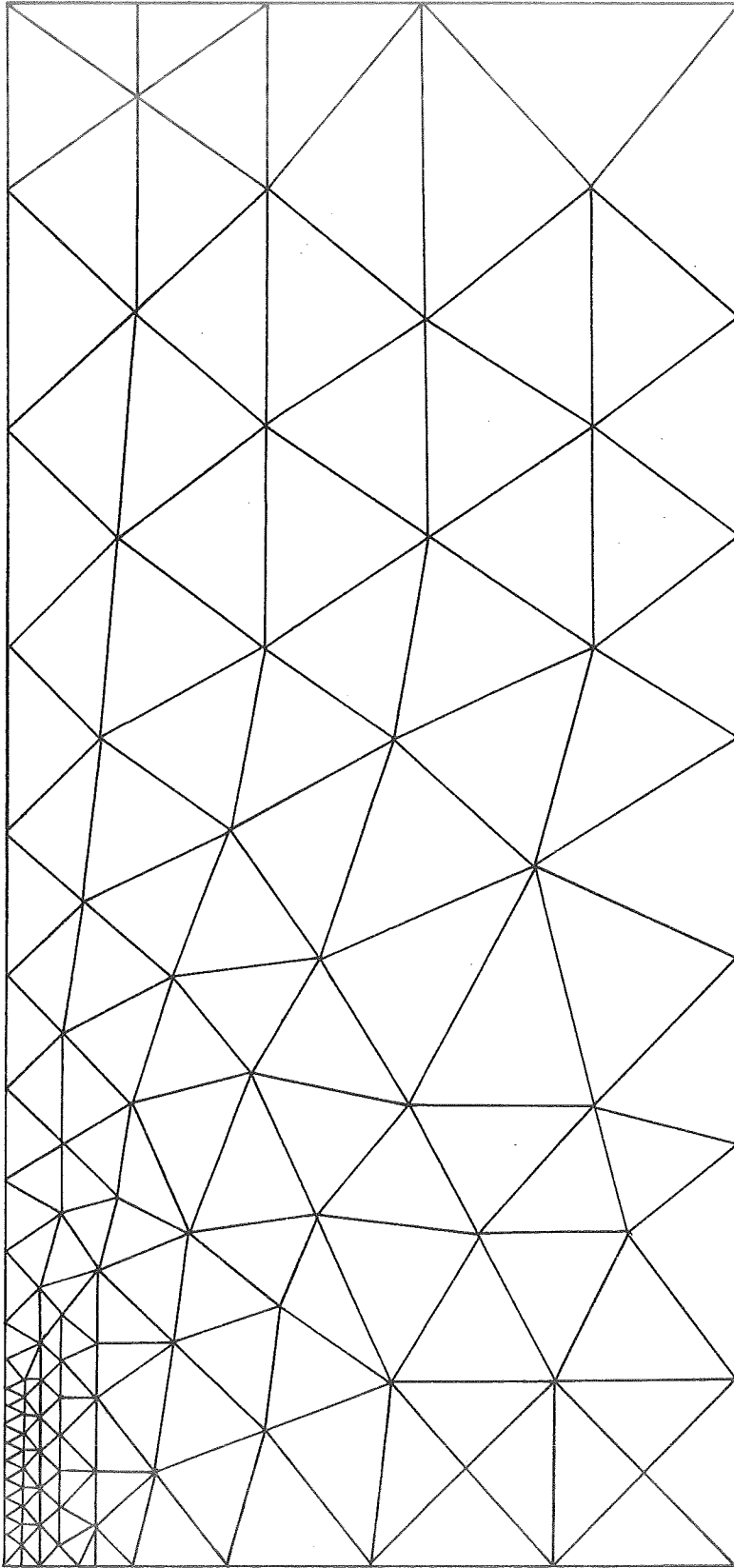


Figure 22. Axisymmetric Finite Element Model of a Propellant Grain

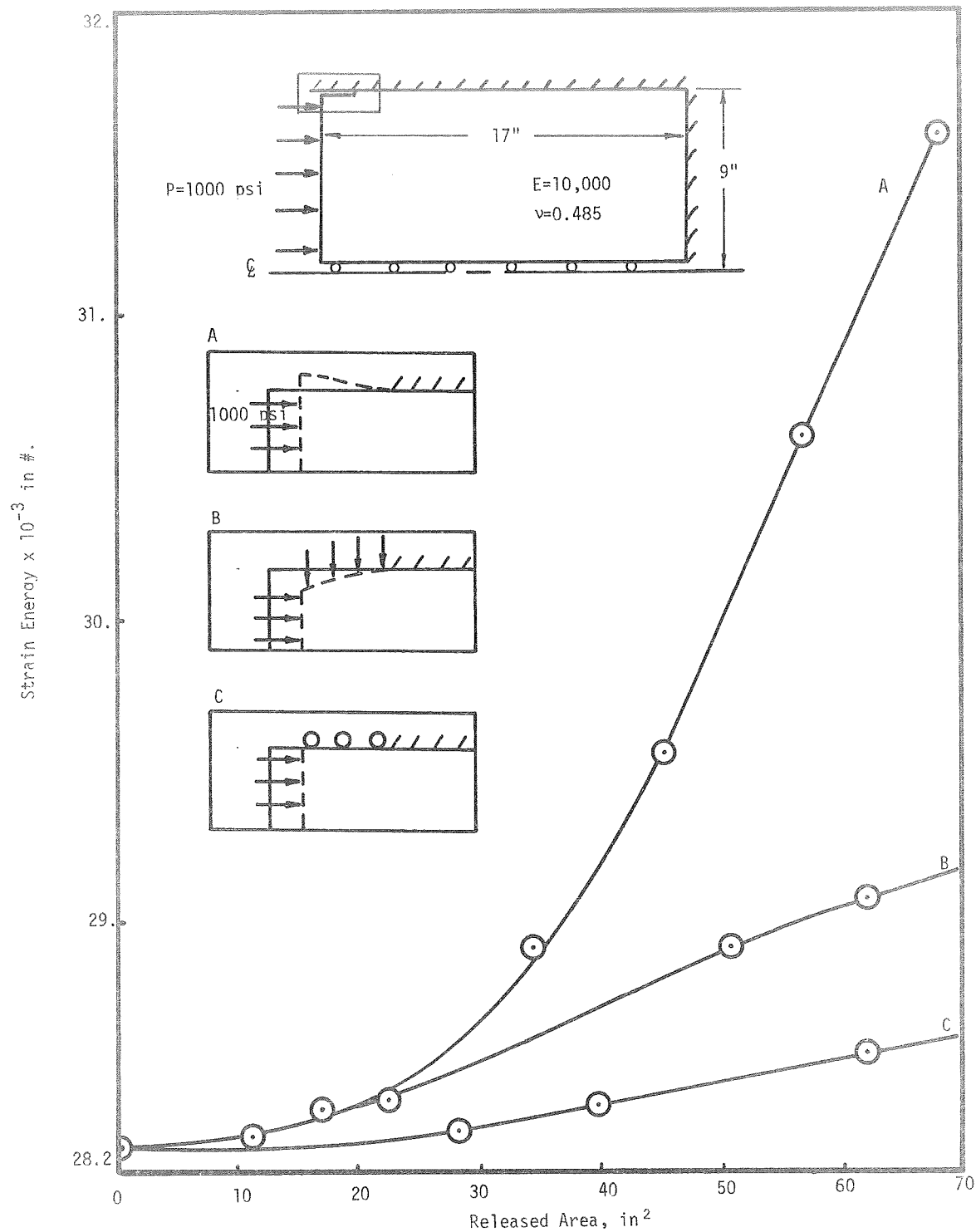


Figure 23 Strain Energy vs. Area for Various End Conditions

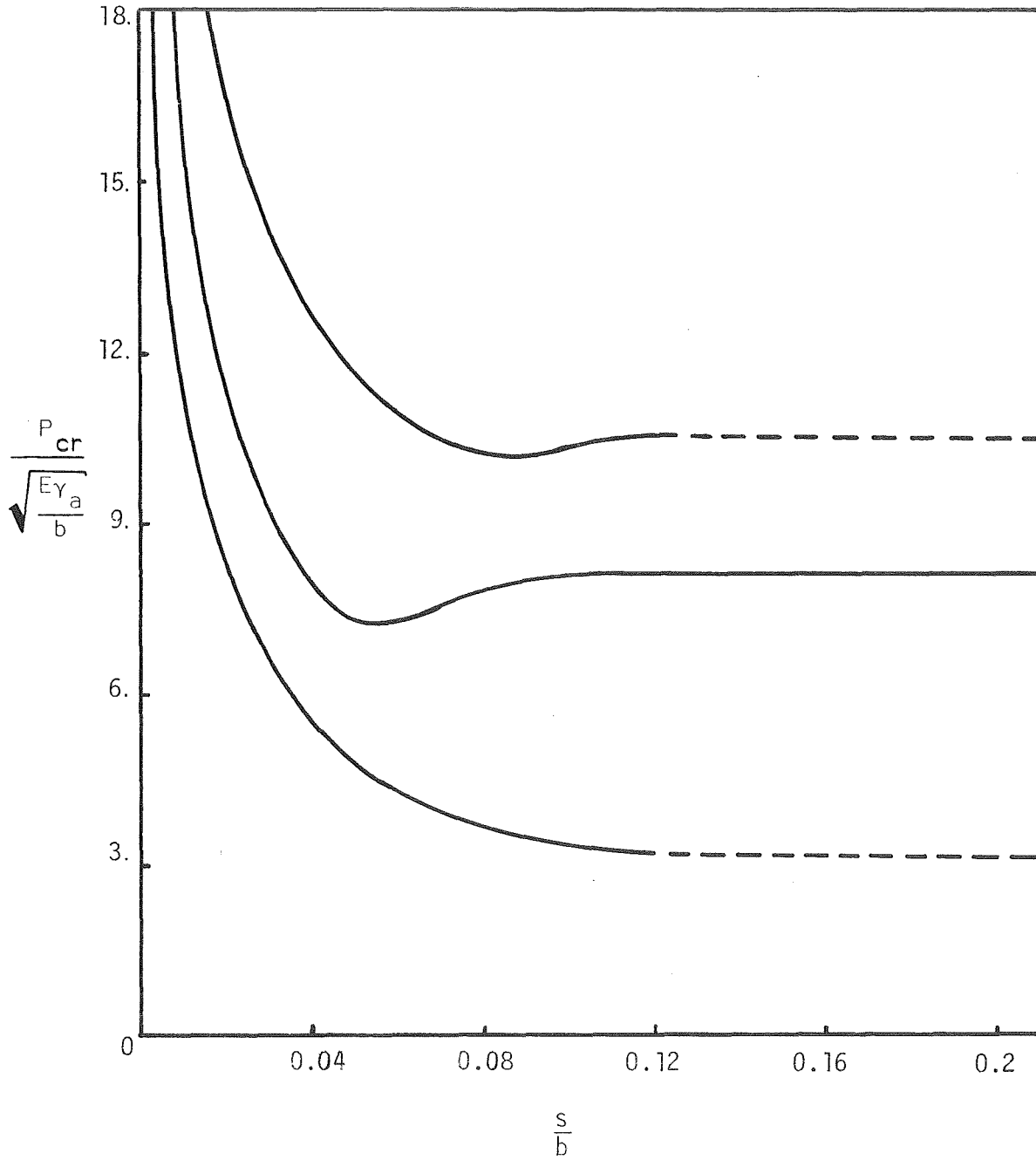


Figure 24. Critical pressure vs. crack length for bond failure

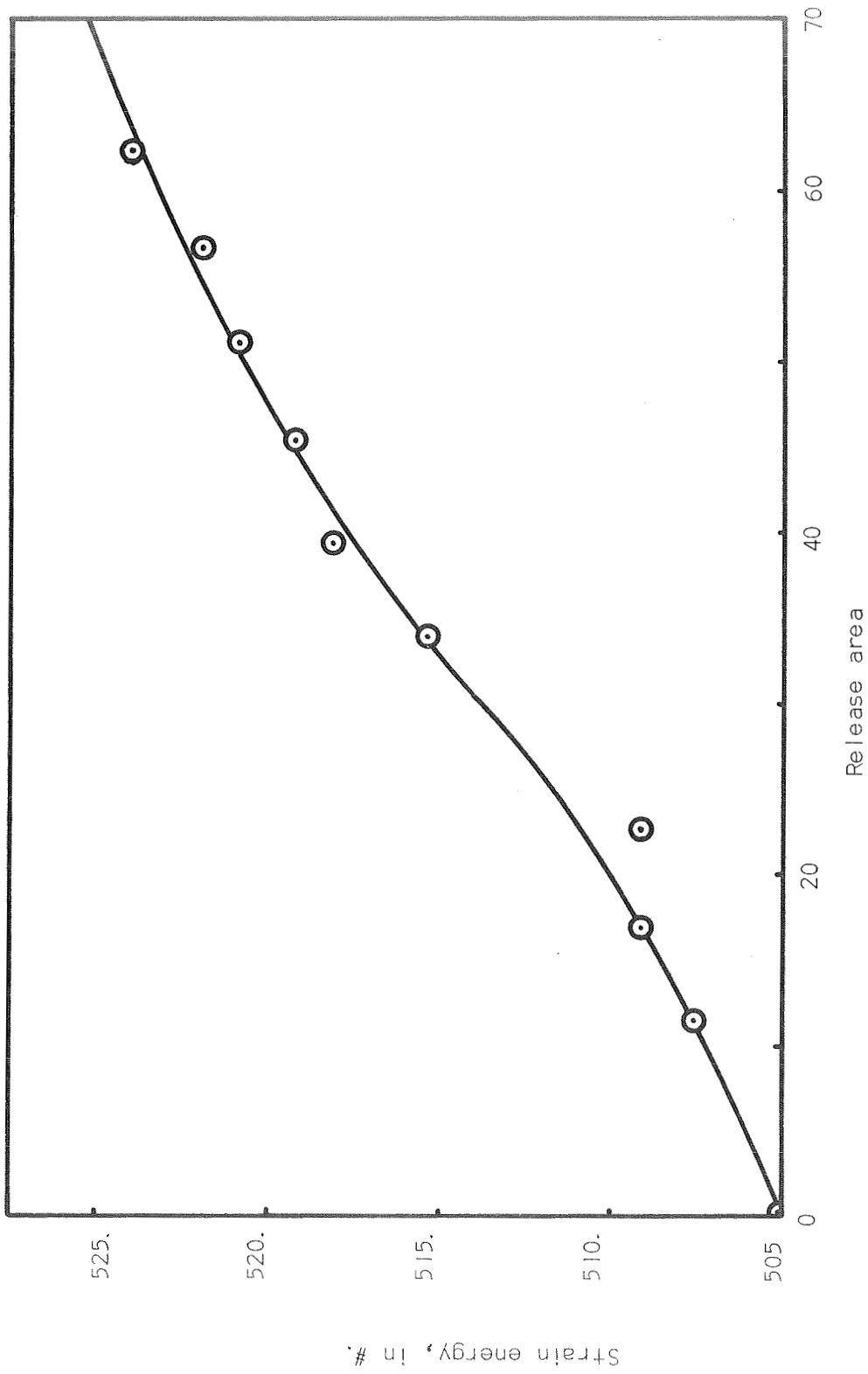


Figure 25. Strain Energy versus Area for Acceleration Loading

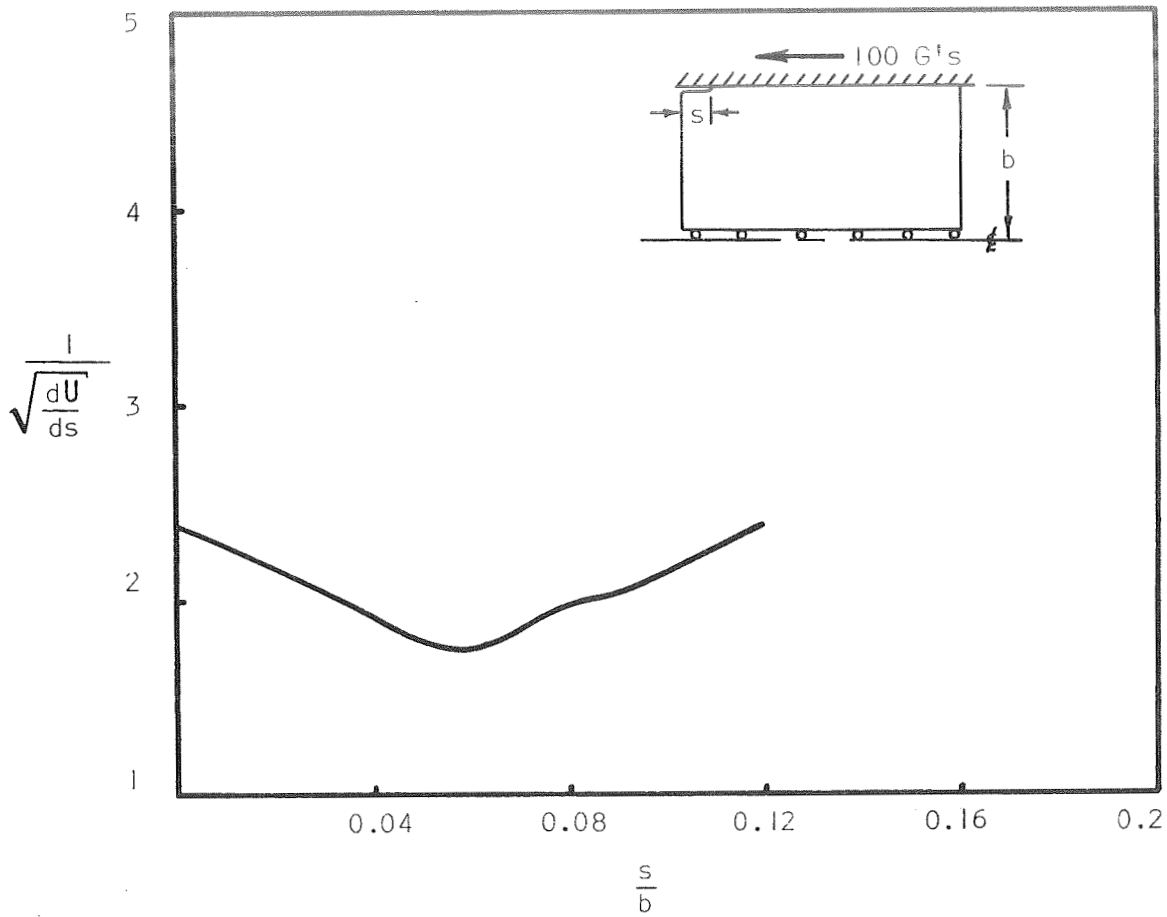


Figure 26. Inverse square root of energy release rate for acceleration loading

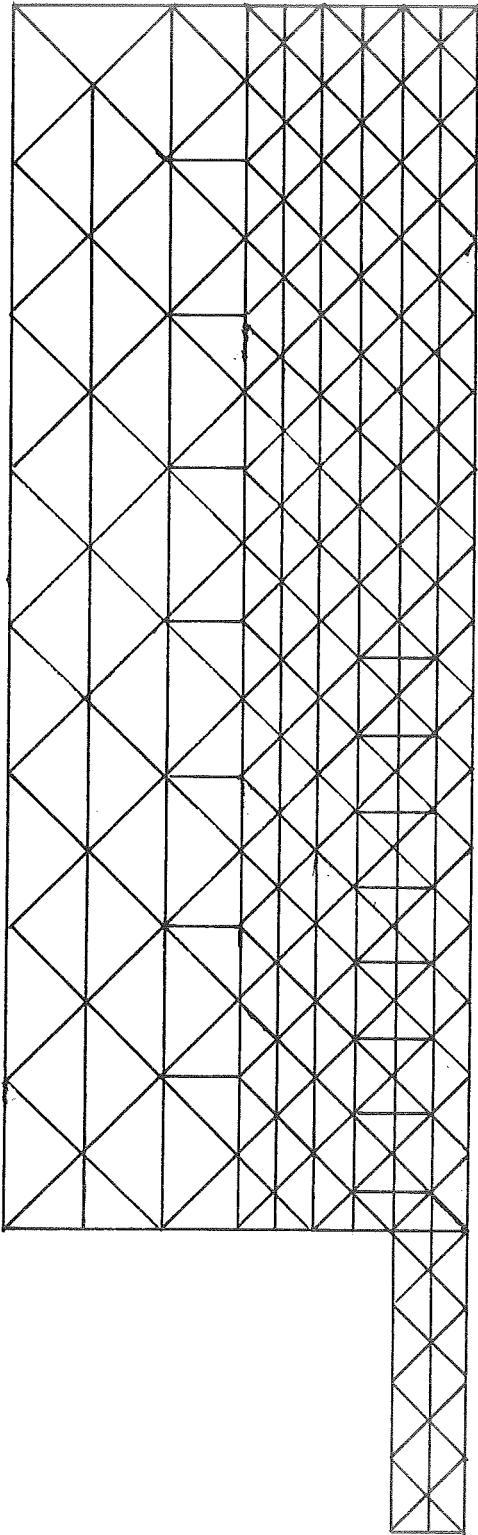


Figure 27. Finite element grid for fiber pull out problem

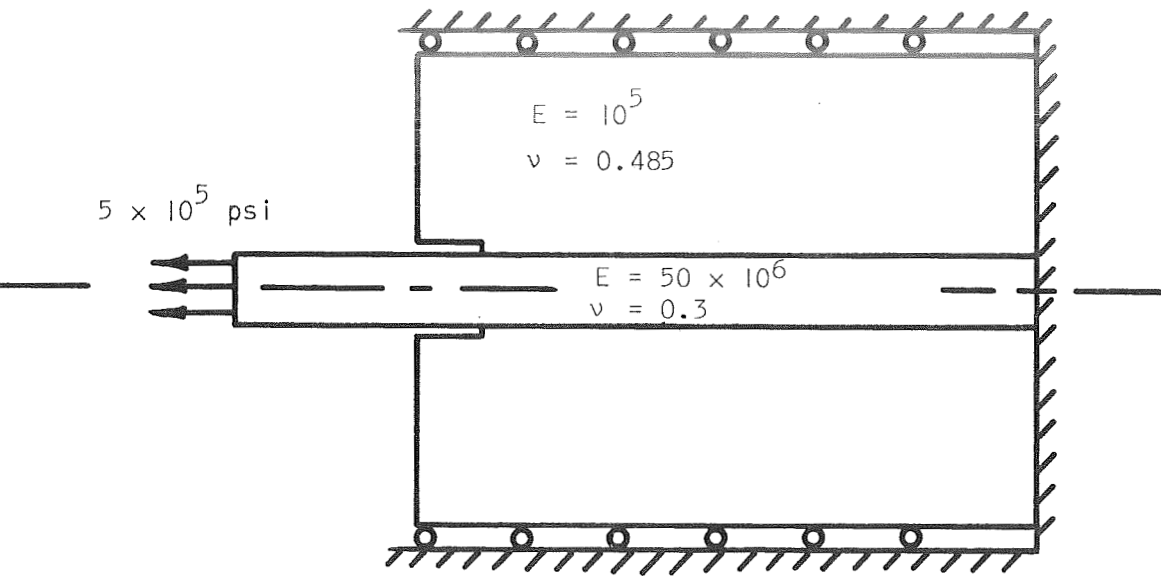


Figure 28. Schematic of area release on filament problem

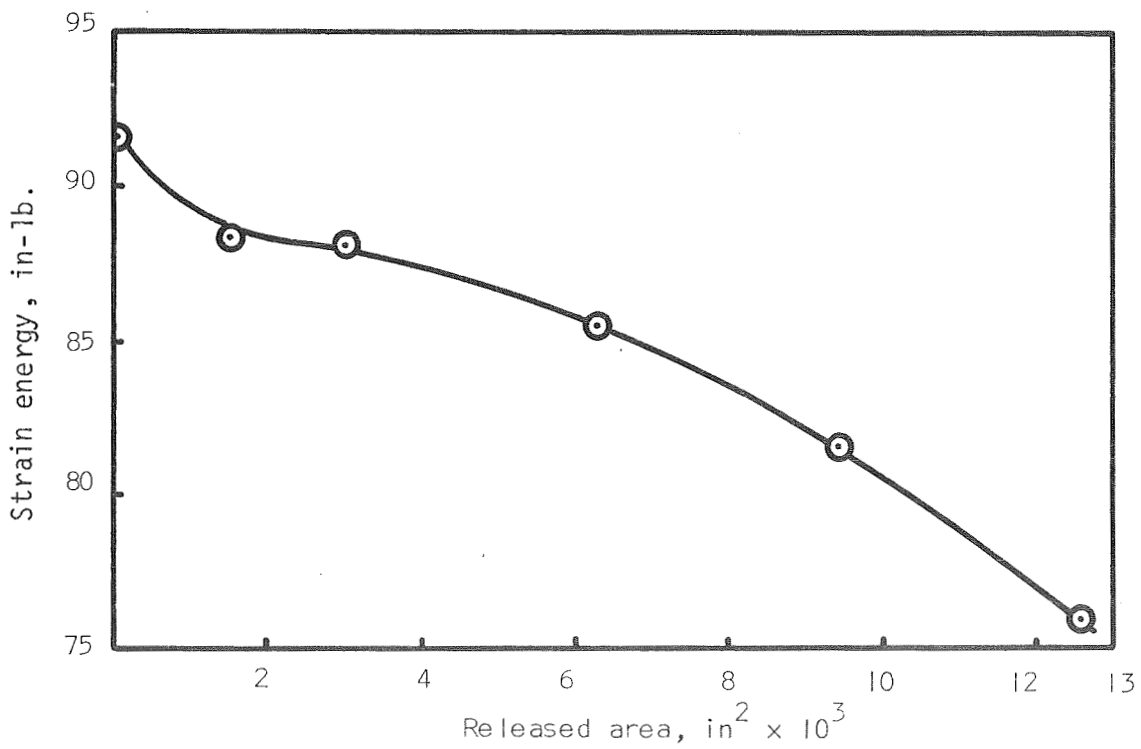


Figure 29. Strain energy versus release area on filament problem

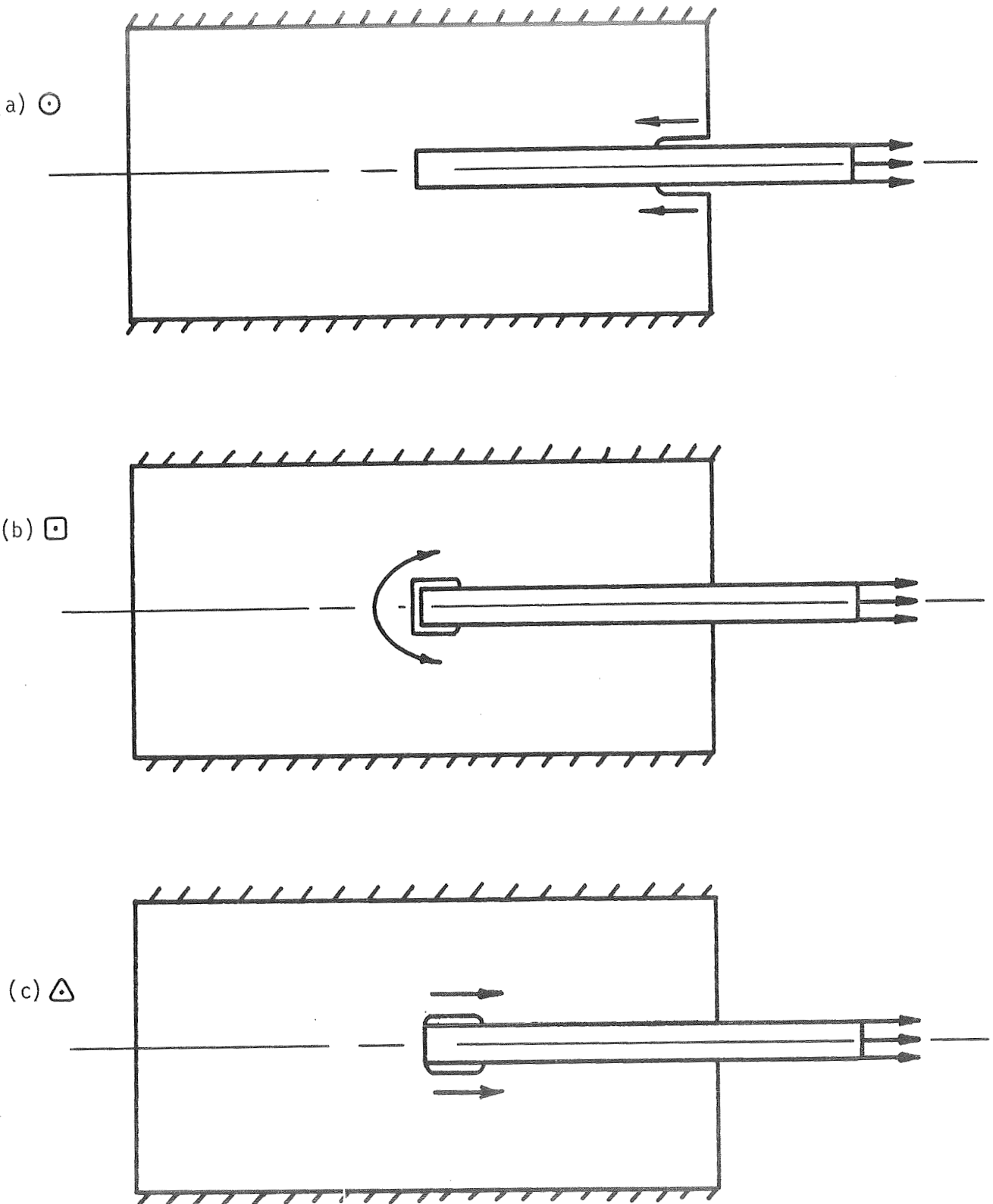


Figure 30. Profile of Hypothesized Unbonds in axisymmetric body

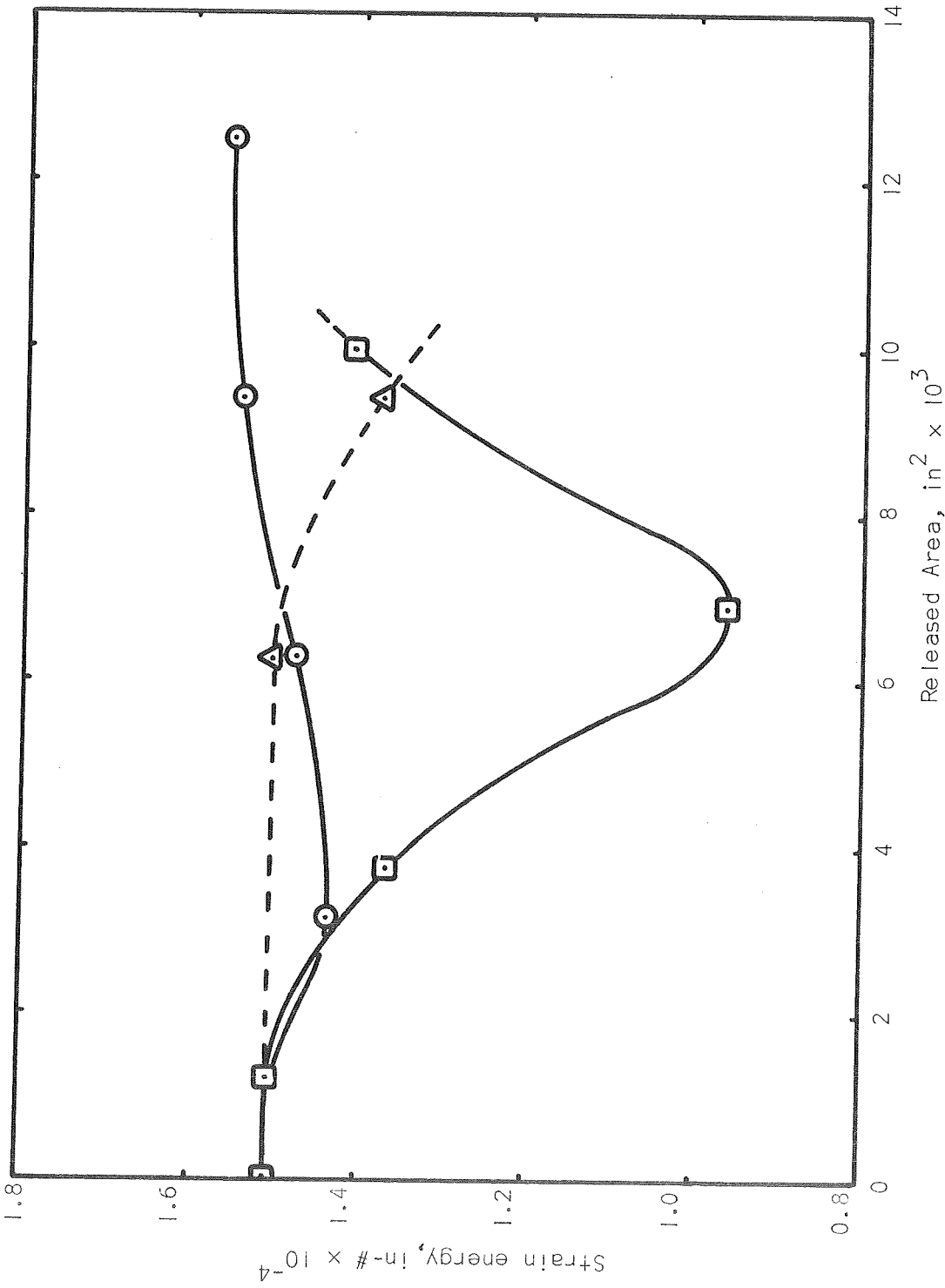


Figure 31. Energy release for the fiber pull out problem

VITA

Name	William Benjamin Jones, Jr.
Age	32
Education	B.S.M.E. Texas Technological College 1959 M.S.M.E. Texas Technological College 1960 Ph.D. University of Utah 1970
Honors	A.S.M.E. Student Paper Award, 1958
Experience	
Teaching	Teaching Fellow, Texas Technological College 1959-1960
Research	Research Assistant, N.A.S.A. Contract on Cumulative Damage in Viscoelastic Materials University of Utah 1966-1969
Industrial	Senior Engineer, Rocketdyne, A Division of North American Rockwell, Inc., Solid Rocket Division, McGregor, Texas 1960-1966
Publications	"Viscoelastic Vibrations," J. D. Burton and J. D. Frazee (co-authors) Bulletin of the 3rd Meeting of the ICRPG Working Group on Mechanical Behavior, CPIA Publication No. 61u, October 1964. "Cumulative Damage in the Mechanics of Viscoelastic Fracture," M. L. Williams and F. R. Wagner (co-authors) Bulletin of the 6th Meeting of ICRPG Working Group on Mechanical Behavior, CPIA Publication No. 158, Vol. 1, October 1967. "A Simple Test for Certain Cases of Adhesion," Presentation at the American Chemical Society, Rubber Division Meeting, April 1969.

Publications (continued)

"Secondary Crack Trajectory," E. R. Simonson, (co-author) submitted to the International Fracture Mechanics Journal, August 1969.

"Some Recent Advances in Adhesive Fracture Analysis," M. L. Williams (co-author), to be published in Bulletin of 1st Annual JANNAF Mechanical Behavior Working Group Meeting, November 1969.

Plus numerous internal reports.